# Impact of the Tibetan Plateau on Global High-Frequency Temperature Variability

Zifan Su,[a,b] Yongkun Xie,[a] Jianping Huang,[a] Guoxiong Wu,[c,d] Yuzhi Liu,[a] and Xiaodan Guan[a]

[a] Collaborative Innovation Center for Western Ecological Safety, Lanzhou University, Lanzhou, China
[b] College of Atmospheric Sciences, Lanzhou University, Lanzhou, China
[c] State Key Laboratory of Numerical Modeling for Atmospheric Sciences and Geophysical Fluid Dynamics, Institute of Atmospheric Physics, Chinese Academy of Sciences, Beijing, China
[d] College of Earth and Planetary Sciences, University of Chinese Academy of Sciences, Beijing, China

ABSTRACT: The Tibetan Plateau's (TP) topography has long been recognized for its impact on climate. However, recognition of the influence of the TP on global weather variability remains insufficient. Therefore, this study used numerical simulations to demonstrate the influences of the TP and its mechanical and thermal forcing on global high-frequency temperature variability and eddy kinetic energy (EKE). Despite local influences, the TP influenced the high-frequency temperature variability in far-flung regions like North America. In summer, the TP's influence on high-frequency temperature variability showed dipole patterns in Eurasia and tripole patterns in North America, which were mainly induced by TP thermal forcing. In winter, the TP's influence on high-frequency temperature variability was dominated by mechanical forcing and was less significant for remote regions than in summer. Mechanical forcing dominated EKE in both summer and winter. Furthermore, the horizontal temperature advection dominated the TP's influence on high-frequency temperature variability for both its thermal effect in summer and its mechanical effect in winter, wherein EKE, as the dynamical factor, determined the horizontal temperature advection rather than the thermodynamical factor, the temperature gradient. Our findings suggest that the TP, via its mechanical and thermal forcing, may have an impact on temperature-related weather extremes around the world.

SIGNIFICANCE STATEMENT: The Tibetan Plateau (TP), being one of the world's largest topographies, has been demonstrated to influence both paleoclimatic evolution and contemporary climate variability. However, the effect of TP on global weather variability has not been thoroughly studied. Therefore, this study looked into the effect of the TP on global high-frequency temperature variability. The TP's overall, mechanical, and thermal effects on high-frequency temperature variability and EKE were specifically demonstrated. To get insights into dynamics, the physical processes underpinning the TP's influence on high-frequency temperature variability were further clarified. This study contributes to a better understanding of the effects of large-scale topography on global high-frequency temperature variations, as well as relevant weather extremes.

KEYWORDS: Dynamics; Topographic effects; Diabatic heating; Temperature; Synoptic-scale processes; Climate models

## 1. Introduction

Located in the subtropics of the Eurasian continent, the Tibetan Plateau (TP) influences both local and remote climates (Queney 1948; Yeh 1950; Manabe and Broccoli 1990; Molnar et al. 2010; Liu et al. 2020; Huang et al. 2023). The TP can influence the climate through atmospheric circulation, including disturbances in westerlies, Rossby waves, and zonal- or meridional-vertical overturning circulation cells (Bolin 1950; Held and Ting 1990; Lin and Wu 2011; Liu et al. 2017; Zhao et al. 2019; Xie et al. 2023a). These atmospheric circulations can further interact with the oceans, thus provoking additional influences on the climate through air–sea interactions. For example, the geologic uplift of the TP topography has been suggested to facilitate the establishment of the Atlantic meridional overturning circulation (Fallah et al. 2016; Su et al. 2018; Yang and Wen 2020). The TP can also influence the air–sea interactions over the Indian, Pacific, and Atlantic Oceans (Baldwin et al. 2019; Sun et al. 2019; He et al. 2019; Z. Wang et al. 2019; Xie et al. 2023b). These air–sea interactions are provoked by TP-induced global-scale heat and moisture transport and anomalous atmospheric circulations, as well as local wind–evaporation–sea surface temperature (SST) and cloud–shortwave radiation–SST feedback (Xie et al. 2023b). The remote influence of the TP can even reach the Arctic and Antarctic (Wang et al. 2023; Xie et al. 2023c).

Besides climate, studies have demonstrated that the TP can influence extreme weather events. For example, TP snow cover can influence interannual variations in Eurasian heatwaves through atmospheric teleconnections and local feedback among high-pressure anomalies, cloud cover, and boundary layers (Wu et al. 2016). Moreover, high-potential vorticity systems formed over the TP and traveling downstream can favor extreme precipitation in China (Xiang et al. 2013; Li et al. 2020; Li and Zhang 2023). Through the generation and eastward advection of potential vorticity, the TP influenced the severe precipitation

---

event that occurred in January 2008 in southern China (Wu et al. 2020) and contributed to severe flooding along the Yangtze River during the summer of 2020 (Ma et al. 2022).

High-frequency temperature variability is intimately associated with extreme heat or cold occurrences since it is a direct statistical variable demonstrating the deviation of extreme temperatures from the climatological mean (Schär et al. 2004; Rahmstorf and Coumou 2011; Schneider et al. 2015). We use the high-frequency variance of near-surface temperature in this study to statistically characterize temperature variability. Recently, Lutsko et al. (2019) investigated the influence of large-scale topography on wintertime high-frequency temperature variability in the Northern Hemisphere. They suggested that the large-scale topography of the TP reduced the upstream temperature gradients, thereby thermodynamically reducing the upstream high-frequency temperature variability. Meanwhile, the TP topography enhanced the downstream temperature gradients and, thereby, the downstream high-frequency temperature variability. Regarding the dynamical influence on high-frequency temperature variability, TP topography can weaken downstream transient eddies by disturbing the recycling of energy from upstream eddies. Nonetheless, Lutsko et al. (2019) investigated only the wintertime situation and did not separately analyze the mechanical and thermal effects of the TP. Therefore, these untouched aspects are the focus of this study.

To comprehend the mechanisms behind the climate impacts of the TP, it is necessary to distinguish the TP's mechanical and thermal effects from its overall effect (Wu 1984; Held and Ting 1990; Boos and Kuang 2010; Son et al. 2019; Chiang et al. 2020). The mechanical effect represents the influence of the TP topography on the climate when diabatic heating over the TP is constant. The thermal effect refers to the isolated influence of diabatic heating over the TP on the climate. The mechanical effects mainly involve TP-topography-deflected flows, orographic-forcing-induced Rossby waves, and gravity wave drag (Bolin 1950; Held and Ting 1990; Lutsko and Held 2016; Son et al. 2019; Xie et al. 2023a). Thermal effects occur because the TP is a diabatic heating source in summer and sinks in winter in the subtropics of the Northern Hemisphere (Yanai et al. 1992; Ping and Longxun 2001; Wu et al. 2007; Liu et al. 2007).

Case studies have been conducted to explore the impact of the TP on downstream or surrounding extreme weather events (Wu et al. 2020; Ma et al. 2022). However, research examining the TP's impact on global variability remains insufficient. This study used climate model simulations to investigate the overall, mechanical, and thermal influences of the TP on global temperature and circulation on a high-frequency temporal scale. The remainder of this paper is in the following organization. Section 2 introduces the data and methods, as well as validates the performance of the Community Earth System Model (CESM), version 2.1.3 (Danabasoglu et al. 2020), used in this study by comparing the CESM simulations to observations and through intermodel comparison. Section 3 presents the results as follows: section 3a elaborates on the overall, mechanical, and thermal influences of the TP on the high-frequency temperature and circulation variability in boreal summer and winter. Section 3b specifically explains how adiabatic horizontal and vertical temperature modification and diabatic processes contributed to the TP's influence on temperature variability. Section 4 presents the conclusions and discussion.

## 2. Data and methods

### a. Reanalysis data

The fifth major global reanalysis produced by European Centre for Medium-Range Weather Forecasts (ECMWF) (ERA5; Hersbach et al. 2020), Modern-Era Retrospective Analysis for Research and Applications, version 2 (MERRA-2; Gelaro et al. 2017), and National Centers for Environmental Prediction (NCEP) and Department of Energy (DOE) AMIP-II reanalysis (NCEP-2; Kanamitsu et al. 2002) were used in this study to validate the performance of CESM in simulating the observed characteristics of the high-frequency temperature and circulation variability. The variables examined are the high-frequency variance of near-surface air temperature ($\overline{T'^2}$, $T' = T - \overline{T}$) and eddy kinetic energy (EKE) at 500 hPa, where $T'$ denotes the temperature anomaly at each time point relative to the monthly mean value $\overline{T}$ (section 2c).

The ERA5, MERRA-2, and NCEP-2 data are 3-hourly, hourly, and 6-hourly, respectively. The variables employed were 2-m air temperature and 500-hPa zonal and meridional wind speeds. The horizontal resolutions of the ERA5 2-m single-level and pressure-level data are $1° \times 1°$ and $2° \times 2°$, respectively. The horizontal resolution of the MERRA-2 data is $0.5° \times 0.625°$. The NCEP-2 data are in $2.5° \times 2.5°$ and T62 Gaussian ($192 \times 94$) grids for pressure-level and 2-m single-level data, respectively. Note that the original resolutions of ERA5 data are hourly in time and $0.25° \times 0.25°$ in horizontal. We chose the 2-m single-level data in a $1° \times 1°$ grid that were available from the official for better consistency with the CESM outputs in a $0.9 \times 1.25$ grid. The $2° \times 2°$ gridded and 3-hourly, instead of hourly, ERA5 pressure-level data were used to save storage space. In addition, the models used to produce the ERA5, MERRA-2, and NCEP-2 data have 137, 72, and 28 vertical levels, respectively.

### b. Numerical simulations and models

To separate the overall, mechanical, and thermal effects of the TP on the high-frequency temperature and circulation variability, three sets of numerical experiments were designed: historical simulation as the control (CTRL) run, no TP (noTP) topography, and with TP topography but no diffusive sensible heating over the TP (TPnosh) as the two sensitivity runs. In this way, CTRL − noTP, TPnosh − noTP, and CTRL − TPnosh differences represent the overall, mechanical, and thermal effects of the TP, respectively. We conducted the experiments using CESM, version 2.1.3 (Danabasoglu et al. 2020), which is provided by the National Center for Atmospheric Research (NCAR) and the University Corporation for Atmospheric Research (UCAR). The CESM model has a $0.9 \times 1.25$ finite volume grid ($192 \times 288$) and 32 vertical levels for the atmosphere component (Table 1).

TABLE 1. Information on models and experimental designs.

| Models | | |
| --- | --- | --- |
| Name | Resolution | Institute |
| CESM (2.1.3) | Official tag: f09_f09_mg17 Atmos: CAM6, 0.9 × 1.25 finite volume grid; 192 × 288 lat/lon; 32 vertical levels | NCAR and UCAR/ United States |
| FGOALS-f3-L | Atmos: FAMIL2.2, c96 finite volume grid; 180 × 360 lat/lon; 32 vertical levels | IAP-LASG/China |
| FIO-ESM-2-0 | Atmos: CAM4, 0.9 × 1.25 finite volume grid; 192 × 288 lat/lon; 26 vertical levels | FIO/China |

| CESM experiments | | | |
| --- | --- | --- | --- |
| Name | Experimental design | Integration time | Model |
| CTRL | The historical run commences from 1 Jan 1850, with the external forcing defined by the observed values. | 1979–2014 (3-hourly outputs for 2000–14) | CESM (2.1.3) |
| noTP | The topography is modified by setting surface elevations to 500 m for the Asian topographies above 500 m. | | |
| TPnosh | Modified from CTRL by directly setting diffusive sensible heat at all the model levels over the regions with modified topographies in the noTP experiment to zero. | | |

| GMMIP experiments | | | |
| --- | --- | --- | --- |
| Name | Experimental design | Integration time | Model |
| CTRL | Same as CESM experiments except for integration time. | 1870–2014 | FGOALS-f3-L |
| noTP | Same as CESM experiments. | 1979–2014 | FIO-ESM-2-0 |
| TPnosh | Same as CESM experiments but different in coding with FGOALS-f3-L, which sets the vertical temperature diffusion term to zero in the atmospheric thermodynamic equation at the bottom boundary layer. | | |

The three experiments with prescribed SSTs and sea ice for the period of 1979–2014 are detailed as follows: The CTRL experiment is consistent with the AMIP-historical experiment of the phase 6 of Coupled Model Intercomparison Project (CMIP6; Eyring et al. 2016), in which the model forcings are based on the observed greenhouse gas emissions, land-use conditions, solar forcing, and other variables from 1979 to 2014. In accordance with the Global Monsoon Model Intercomparison Project (GMMIP; Zhou et al. 2016), the noTP experiment is based on the historical experiment but sets surface elevations to 500 m for the regions of Asian topographies above 500 m. The TPnosh experiment maintains the same topography as the historical experiment but adjusts diffusive sensible heat to zero at all the model levels in each time step of model integration over the same domain as the noTP experiment with modified topographies. Diffusive sensible heat is modified because it is a major component of total heating over the topographies (Yanai et al. 1992; Wu et al. 2007).

It should be noted that the ocean was not actively coupled in the experiments because large topography changes in fully coupled models will cause radical changes in global oceanic overturning circulation, which complicates the dynamics we aimed to investigate by introducing the effects of oceanic circulation and air–sea interactions. Moreover, topography-induced changes in the oceanic overturning circulation take at least several centuries of integration time to reach an equilibrium state (Su et al. 2018; Yang et al. 2020, 2024), which

significantly raises the cost of experiments. As a result of considering both study emphasis and experiment expense, atmosphere-only (land–atmosphere coupling is active) experiments were used. Nonetheless, more research into oceanic circulation and air–sea interactions is warranted. Furthermore, because land–atmosphere interactions are active and the diffusive sensible heat was changed in each model time step of the TPnosh experiment, all atmosphere and land feedbacks that regulate total diabatic heating of the atmosphere were fully active (Lagüe et al. 2019; Xie et al. 2023b). The codes used to run the CESM experiments are available to the public via the link provided in the *data availability statement*.

In all three experiments, monthly mean outputs were archived throughout the 1979–2014 period, while 3-hourly outputs were only retained for the 15 years from 2000 to 2014. The 3-hourly outputs were used to calculate high-frequency temperature variability and EKE. Only 15-yr and 3-hourly, instead of hourly, outputs were used to minimize storage capacity. The monthly outputs were used to obtain the mean temperature gradient and other basic climate variables. The GMMIP also provides the monthly outputs of the three experiments we performed, but only outputs from two models, FGOALS-f3-L (He et al. 2020) and FIO-ESM-2-0 (Bao et al. 2020), are available (Table 1).

When the climatology of high-frequency temperature variance and EKE in the CESM control run was compared to that of the ERA5, MERRA-2, and NCEP-2 data (Figs. A1 and A2),
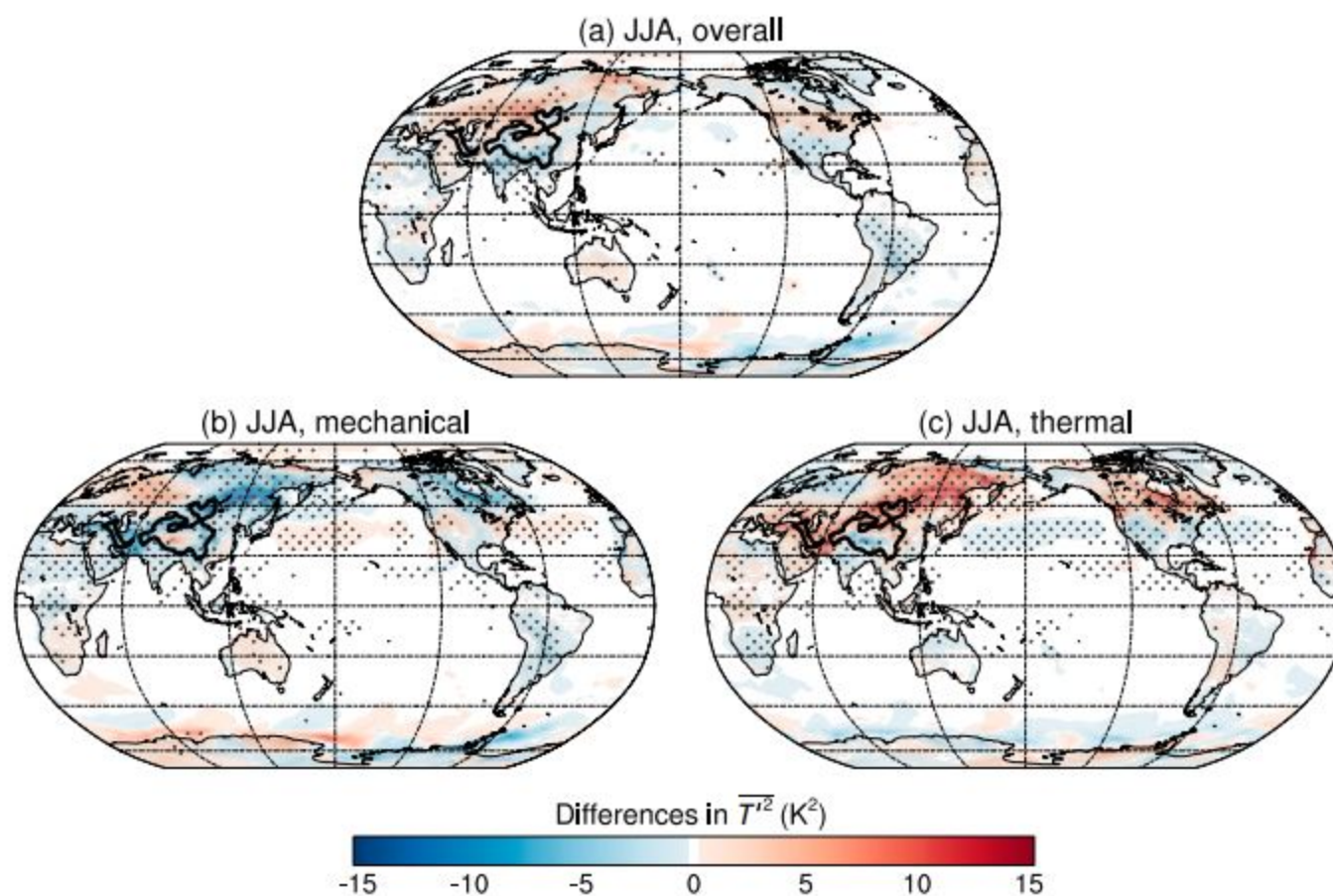
FIG. 1. Differences in the high-frequency variance of near-surface air temperature $[\overline{T'^2}$; Eq. (1)] in JJA based on CESM (version 2.1.3) for 2000–14, determined using simulations (a) CTRL − noTP, (b) TPnosh − noTP, and (c) CTRL − TPnosh, which represent the overall, mechanical, and thermal effects of the TP, respectively. The dots indicate statistical significance at the 95% confidence level. The black contour indicates 1.5 km of elevation.

it was discovered that CESM performed well in mimicking the observed characteristics of variability. The spatial patterns of high-frequency temperature variance in the CESM control run match those found in the reanalysis data (Fig. A1). Furthermore, the simulated EKE from CESM and those observed exhibit a consistent spatial pattern (Fig. A2), with the NCEP-2 showing a weaker magnitude of EKE along storm tracks than the ERA5 and MERRA-2 data, as well as the CESM control run. Detailed comparisons of CESM simulations and observations can be found in appendix A. Although the spatial resolutions of pressure-level data are closer between ERA5 and NCEP-2, the spatial features of EKE are closer between ERA5 and MERRA-2 rather than NCEP-2. ERA5 and MERRA-2 also have different temporal resolutions but still show great consistency. Therefore, the results are not sensitive to spatial and temporal resolutions (not susceptible to employing outputs of 3 hourly or hourly, in a $1° × 1°$ grid or finer grids). The consistency among the results from the two GMMIP models and CESM was further examined to verify the performance of CESM in simulating the overall, mechanical, and thermal effects of the TP on basic climate variables. The CESM and GMMIP simulations agreed well on the three effects of the TP on temperature and geopotential height (Fig. A3). In conclusion, the great skill of CESM in reproducing both observed high-frequency temperature and circulation variability and the three effects of the TP on basic climate variables demonstrates the dependability of the CESM simulations for further investigation.

### c. High-frequency temperature and circulation variability

The high-frequency variance of the near-surface air temperature ($T$) and EKE at 500 hPa was used to quantify the high-frequency temperature and circulation variability. The high-frequency variance was calculated from 3-hourly data as follows: The monthly variance of near-surface air temperature [i.e., $\overline{T'^2}$, Eq. (1)] was calculated from 3-hourly data; the monthly variance was averaged over boreal summer [June–August (JJA)] and winter [December–February (DJF)] in each year; the climatological average was calculated over the 15-yr period from 2000 to 2014. Similarly, the EKE was obtained by calculating the high-frequency variance of the wind velocity in the zonal and meridional directions, i.e., $u$ and $v$ [Eq. (2)] and then taking their seasonal and climatological average.

$$\overline{T'^2} = \frac{1}{n}\sum_{i=1}^{n}(T_i - \overline{T})^2, \tag{1}$$

$$\text{EKE} = \frac{1}{2}\left[\frac{1}{n}\sum_{i=1}^{n}(u_i - \overline{u})^2 + \frac{1}{n}\sum_{i=1}^{n}(v_i - \overline{v})^2\right] \tag{2}$$

where $\overline{T}$, $\overline{u}$, and $\overline{v}$ indicate the monthly means. The number $n$ indicates the number of samples in each month (8 times per day multiplied by the days of the month).

### d. Physical processes underlying high-frequency temperature variability

The terrain-following model-level tendency equation of high-frequency temperature variability, i.e., Eq. (4), was derived to
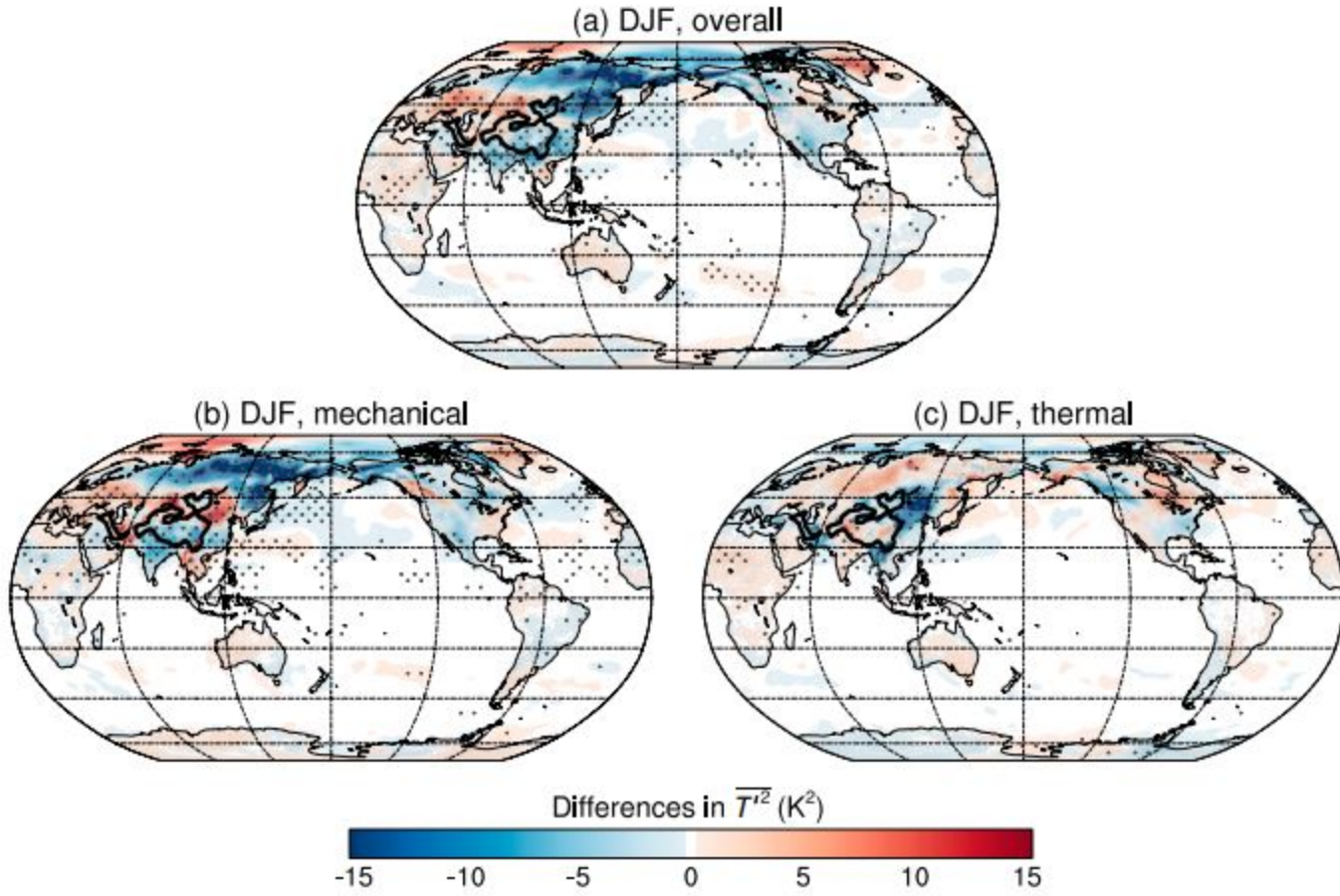
FIG. 2. As in Fig. 1, but for DJF.

quantify the contribution of several physical processes to the high-frequency variance of near-surface air temperature. The derivation is as follows: Take the derivative of the potential temperature equation $T = \theta(p/p_0)^\kappa$ with respect to time, where $p_0 = 1000$ hPa and $\kappa = 0.286$; introduce $dT/dt = \partial T/\partial t + \mathbf{V} \cdot \nabla_h T + \omega_{ml}\partial T/\partial p$ and $\omega_{ml} = \omega - \partial p/\partial t - \mathbf{V} \cdot \nabla_h p$ according to the vertical coordinate transformation rules (Sheng et al. 2021; Xie et al. 2023a), where $\omega = dp/dt$ is the vertical velocity provided in model-level data; combining these equations, we get Eq. (3).

$$\frac{\partial T}{\partial t} = -\mathbf{V} \cdot \nabla_h T + \left(\omega \frac{\kappa T}{p} - \omega_{ml}\frac{\partial T}{\partial p}\right) + \left(\frac{p}{p_0}\right)^\kappa \frac{d\theta}{dt}. \quad (3)$$

Applying a monthly mean to Eq. (3) and subtracting it from the original equation gives the tendency equation for $T'$; multiplying this equation by $2T'$ and repeating the averaging operation, we obtain model-level tendency equation for high-frequency temperature variance as Eq. (4) (see appendix B).

$$\underbrace{\frac{\overline{\partial(T'^2)}}{\partial t}}_{\text{Local}} = \underbrace{-\overline{2T'(\mathbf{V} \cdot \nabla_h T)}}_{\text{adiabatic\_h}} + \underbrace{\overline{2T'\left(\omega \frac{\kappa T}{p} - \omega_{ml}\frac{\partial T}{\partial p}\right)}}_{\text{adiabatic\_v}}$$

$$+ \underbrace{\overline{2T'\left(\frac{p}{p_0}\right)^\kappa \frac{d\theta}{dt}}}_{\text{diabatic}}. \quad (4)$$

The equation indicates that local high-frequency temperature variability is determined by adiabatic horizontal temperature advection (adiabatic_h), adiabatic vertical displacement of air and temperature convection (adiabatic_v), and diabatic processes. The diabatic process exists because of heat exchange with the external environment. With 3-hourly model-level data from CESM simulations, the differences in the three right-hand terms of Eq. (4) between CTRL, noTP, and TPnosh can be used to quantify how the three physical processes contribute to the three effects of the TP on high-frequency temperature variability.

In addition, the horizontal-advection-induced temperature variability is influenced by EKE as the dynamical factor and the mean temperature gradient ($|\nabla_h \overline{T}|$) as the thermodynamical factor. The theoretical considerations are as follows: (i) Changes in the horizontal temperature advection, i.e., $-\mathbf{V} \cdot \nabla_h T$ are determined by changes in the temperature gradient ($\nabla_h T$) and circulation ($\mathbf{V}$). (ii) The gradient of the climatological mean temperature thermodynamically constrains the magnitude of high-frequency temperature advection (Schneider et al. 2015; Lutsko et al. 2019; Dai and Deng 2021; Xie et al. 2022). (iii) EKE is a dynamical factor that indicates the high-frequency variance of circulation. Specifically, the mean temperature gradient at 850 hPa was calculated as follows: gradients of monthly mean 850-hPa temperature in the zonal and meridional directions and their norms were calculated according to Eq. (5) from 2000 to 2014; the gradient norms were averaged over boreal summer and winter for each year; then, the climatological mean was obtained for 2000–14.

$$|\nabla_h \overline{T}| = \sqrt{\left(\frac{\partial \overline{T}}{\partial x}\right)^2 + \left(\frac{\partial \overline{T}}{\partial y}\right)^2}. \quad (5)$$

### e. Statistical method

A two-tailed Student's $t$ test of the differences in the sample means was conducted to evaluate statistically significant
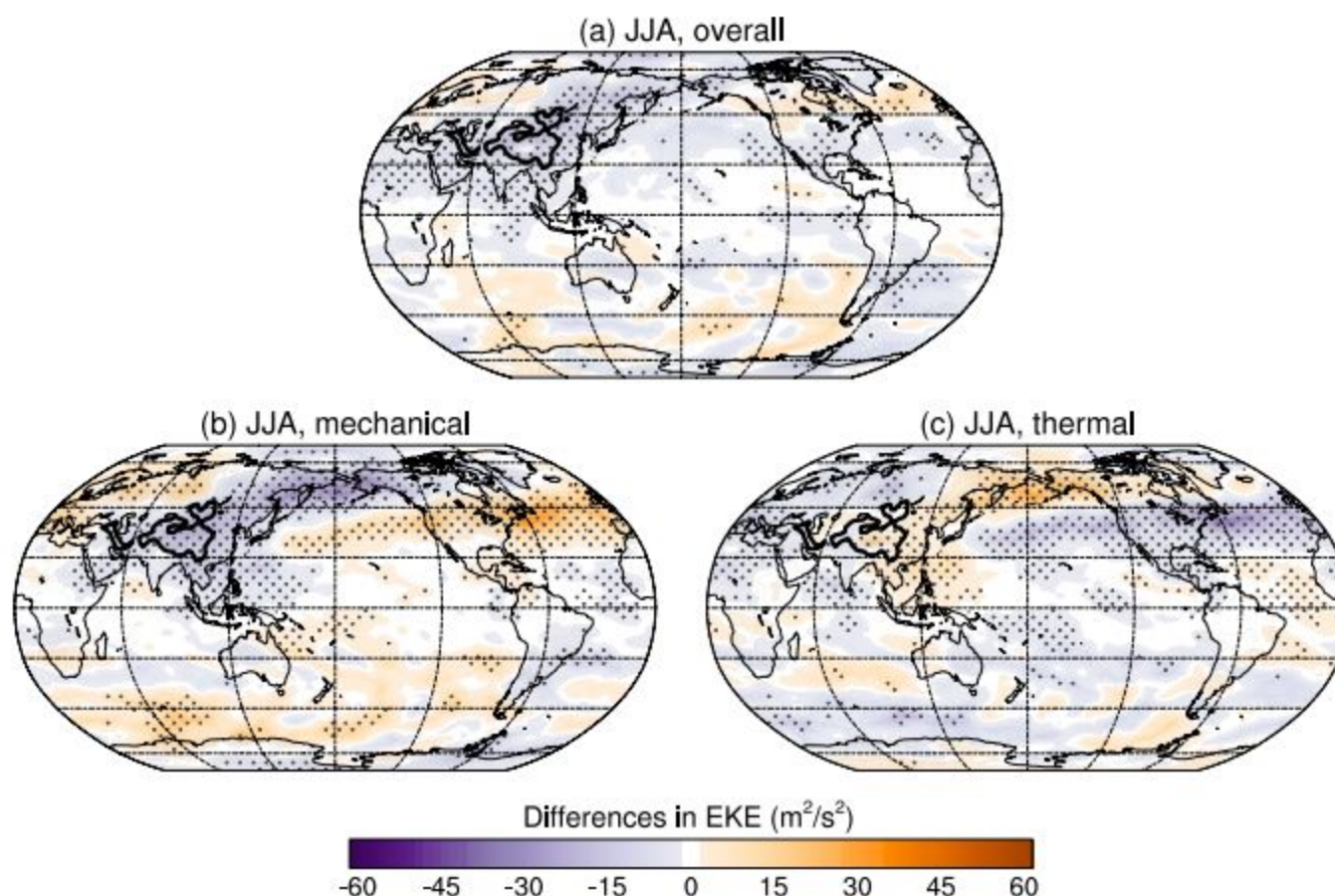
FIG. 3. Differences in the EKE [Eq. (2)] at 500 hPa in JJA based on CESM, version 2.1.3, for 2000–14, determined using simulations (a) CTRL − noTP, (b) TPnosh − noTP, and (c) CTRL − TPnosh, which represent the overall, mechanical, and thermal influences of the TP, respectively. The dots indicate statistical significance at the 95% confidence level. The black contour indicates 1.5 km of elevation.

differences between the control and sensitivity runs. Details of the *t* test are provided (https://www.ncl.ucar.edu/Document/ Functions/Built-in/ttest.shtml) (NCAR 2015). In this study, a *t* test was performed on the yearly time series, which included a sample of 15 individuals for the years 2000–14 or 36 individuals for 1979–2014. The individuals were the JJA mean or DJF mean of each year. A 95% confidence level ($p < 0.05$) was considered statistically significant.

## 3. Results

### a. Overall, mechanical, and thermal influences of the TP on the high-frequency temperature and circulation variability

Besides the overall effect of the TP on the high-frequency temperature and circulation variability, the influences of its mechanical and thermal forcings were separated in the analysis. The TP increased the high-frequency temperature variance over northern Eurasia during boreal summer (Fig. 1a), whereas it decreased the temperature variance over the southern TP and Asian summer monsoon regions. The TP also induced a negative–positive–negative tripole pattern in temperature variance over North America and a negative change over South America. Although signals were observed across Antarctica, they were not statistically significant.

Regarding the individual effects of the mechanical and thermal forcing of the TP, the patterns were roughly opposite (Figs. 1b,c). The increased temperature variance over northern Eurasia was dominated by thermal forcing (Fig. 1) during boreal summer. The reduced temperature variance over the south of the TP was jointly determined by both forcings. Thermal forcing also dominated the tripole pattern over North America, except for a negative change in the north, which was dominated by mechanical forcing. Furthermore, mechanical forcing dominated the negative change in South America. Therefore, thermal forcing dominated the overall influence of the TP on global high-frequency temperature variance except for a few regions in boreal summer.

Unlike the summer, mechanical forcing dominated the overall influence of the TP on temperature variance during boreal winter (Fig. 2). However, similar to the summer, the influence of mechanical forcing was roughly the opposite of that of thermal forcing in boreal winter patterns. As suggested by Lutsko et al. (2019), the TP suppressed the high-frequency temperature variance downstream in boreal winter. The TP also insignificantly suppressed the temperature variance over North America, while enhancing the upstream temperature variance from central Asia to Europe.

Figures 3 and 4 show the influence of TP on the high-frequency variance of atmospheric circulation. In boreal summer, the TP significantly reduced the EKE over regions from the tropics southwest of the TP to the polar region of North America (Fig. 3). Similar to the temperature, a negative–positive–negative tripole pattern of EKE in North America was also observed in boreal summer. However, the influence in the Southern Hemisphere was mostly insignificant. Furthermore,

## (a) DJF, overall



## (b) DJF, mechanical



## (c) DJF, thermal



Differences in EKE (m²/s²)

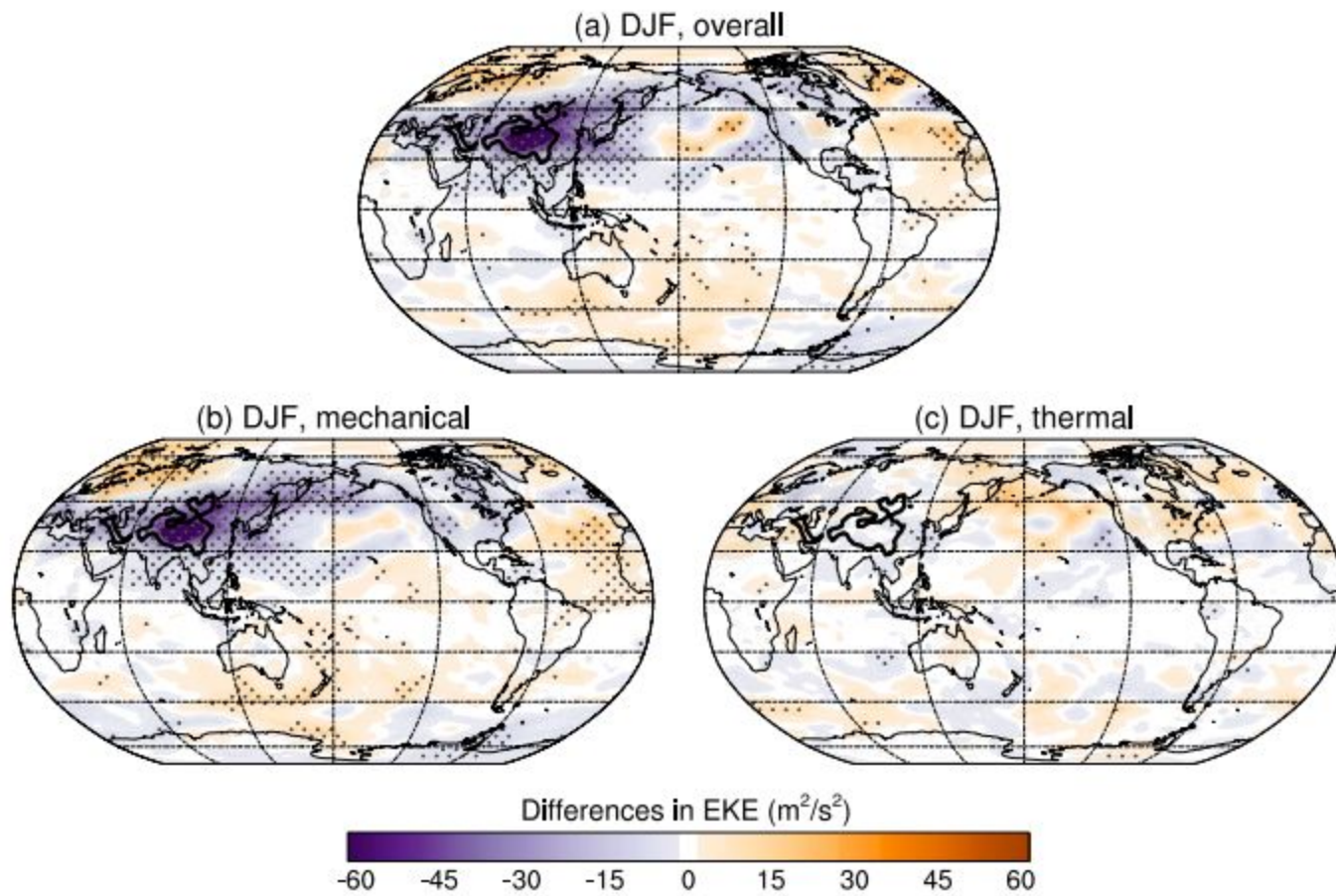-60   -45   -30   -15   0   15   30   45   60

FIG. 4. As in Fig. 3, but for DJF.

the influences of mechanical and thermal forcings on EKE counteracted each other in these patterns. Unlike temperature, which was dominated by thermal forcing, mechanical forcing was dominant in determining the overall influence of the TP on the EKE.

Similar to summer, mechanical forcing dominated the overall influence of the TP on EKE in boreal winter (Fig. 4). However, unlike in the summer, the influence of the thermal forcing of the TP on EKE was minor and insignificant in boreal winter (Fig. 4c). The mechanical forcing of the TP solely determined the overall influence of the TP in boreal winter (Fig. 4), whereas it exerted its dominance by overwhelming the significant and opposite effects of thermal forcing in boreal summer (Fig. 3). The TP significantly reduced the EKE over Eurasia in boreal winter, except for northern Europe and northwestern Russia. In contrast, enhanced EKE was observed over the Nordic seas, its surroundings, and subtropical North Atlantic.

In summary, regardless of temperature and atmospheric circulation, the influences of mechanical and thermal forcings of the TP on the high-frequency temperature and circulation variability generally have opposite patterns. Therefore, the overall influence of the TP on the high-frequency temperature and circulation variability was generally smaller than the individual influences of mechanical and thermal forcings. Mechanical forcing was dominant in the high-frequency variance of temperature in boreal winter and the high-frequency variance of atmospheric circulation in both summer and winter. Thermal forcing was dominant only for high-frequency temperature variance in boreal summer.

### b. Contribution of three physical processes to the TP's influence on high-frequency temperature variability

High-frequency temperature variability influenced by adiabatic horizontal temperature advection, adiabatic vertical-motion-induced temperature modification, and diabatic processes, as indicated by Eq. (4), was examined separately for the overall, mechanical, and thermal effects. The residual is three orders less than other processes in magnitude (Fig. B1), indicating the high accuracy of the model-level tendency equation of high-frequency temperature variability used in this study. The TP had its strong impacts on high-frequency temperature variability from all three physical processes both in boreal summer and winter, and the influences extended to regions far from the TP across the Northern Hemisphere (Figs. 5–7).

During boreal summer (Figs. 5a,c,e), the horizontal temperature advection produced increased temperature variability over Europe (Fig. 1a); the vertical-motion-induced temperature modification and diabatic process led to increased temperature variability over northeastern Asia. The suppressed temperature variability over India, the tripole pattern over North America, and the lower temperature variability in South America (Fig. 1a) were dominated by the horizontal temperature advection, whereas the vertical-motion-induced temperature modification exerted opposite effects (Figs. 5a,c). Furthermore, the lower temperature variability along the southwestern United States and western Mexico and along the western coast of South America should be attributed to the diabatic process (Fig. 5e). Changes in temperature variance around Antarctica were also noticeable but they did not pass the significance test for the majority of the regions.
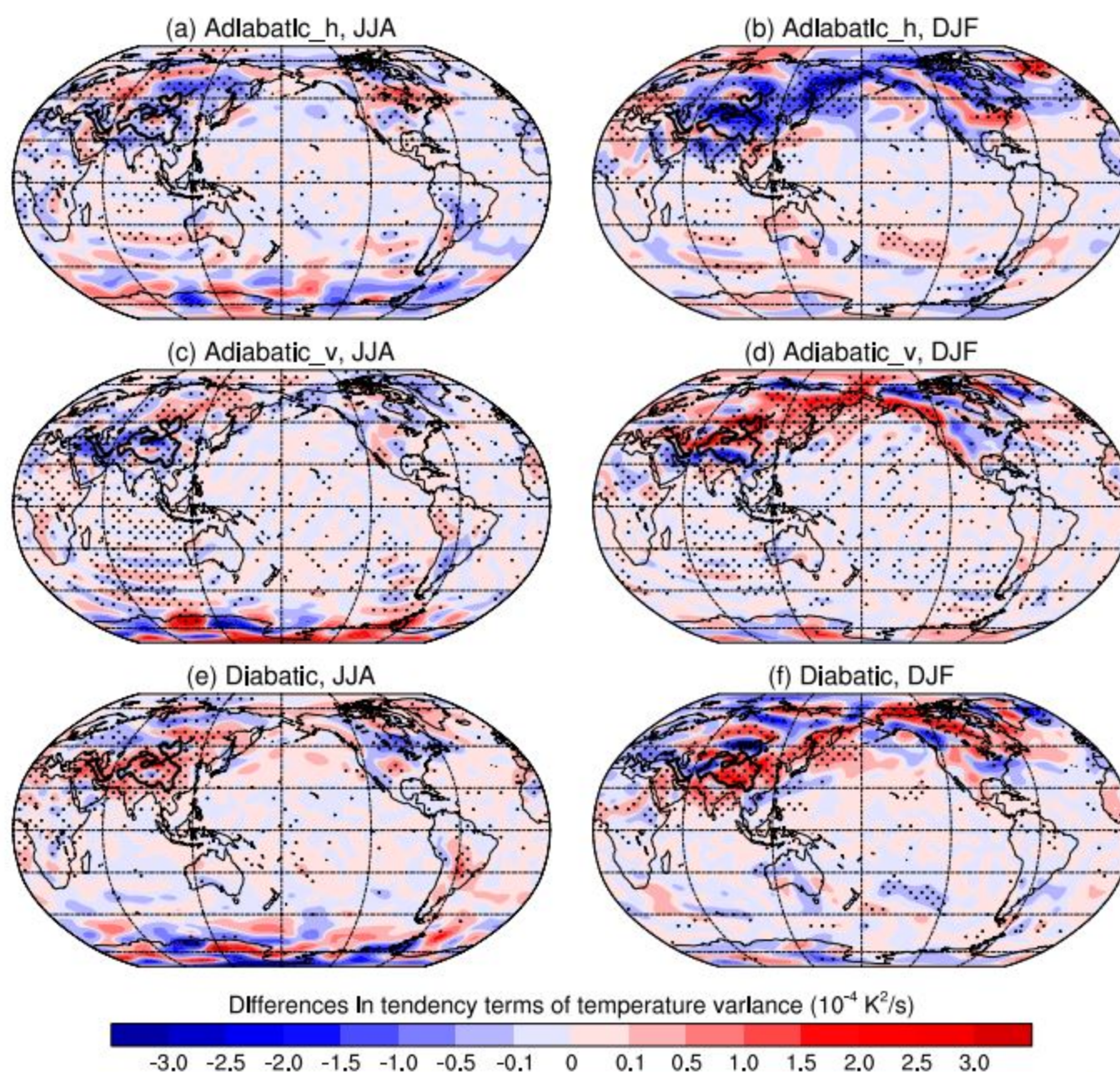
FIG. 5. Differences in the tendency terms of the high-frequency variability of near-surface air temperature [Eq. (4)] in JJA based on CESM, version 2.1.3, for 2000–14, determined using simulations CTRL − noTP, which represents the overall effect of the TP. (a) Adiabatic_h, (c) adiabatic_v, and (e) diabatic processes–induced changes in tendency of the high-frequency temperature variability. (b),(d),(f) As in (a),(c),(e), but for DJF. The dots indicate statistical significance at the 95% confidence level. The black contour indicates 1.5 km of elevation.

During boreal winter (Figs. 5b,d,f), the horizontal temperature advection dominantly resulted in the dampened temperature variability over Siberia, northeastern Asia, and downstream East Asia and the enhanced variability upstream of the TP (Fig. 2a). The negative change in temperature variability over North America was also dominated by horizontal temperature advection, while the other two processes had secondary contributions. Decreased variability in India was solely explained by horizontal temperature advection. Therefore, horizontal temperature advection is the dominant process underlying the overall effect of the TP on high-frequency temperature variability.

Regarding the mechanical effect of the TP (Fig. 6), while the diabatic process favored an increase in temperature variability to the northeast of the TP during boreal summer, horizontal temperature advection offset that and caused suppressed variability there (Fig. 1b). This is also the case for the increased variability

in Europe (Figs. 6a,e). The negative change in the temperature variability over the far north of North America, part of the tripole pattern (Figs. 1a,b), was also induced by the horizontal temperature advection. The decreased temperature variability over South America, dominated by mechanical effect (Fig. 1), was from all three processes. During boreal winter, the reduction in temperature variability over Siberia (Fig. 2b) was dominated by the horizontal temperature advection (Figs. 6b,d,f), which is consistent with Lutsko et al. (2019). Weakened temperature variability over India, dominated by mechanical effect in winter (Fig. 2), and decreased variability in North America were also attributed to the horizontal temperature advection. Above all, the results indicate that the horizontal temperature advection had a major contribution to the mechanical effect of the TP on high-frequency temperature variability.

Regarding the thermal effect of the TP (Fig. 7), the horizontal temperature advection imposed a greater impact on temperature
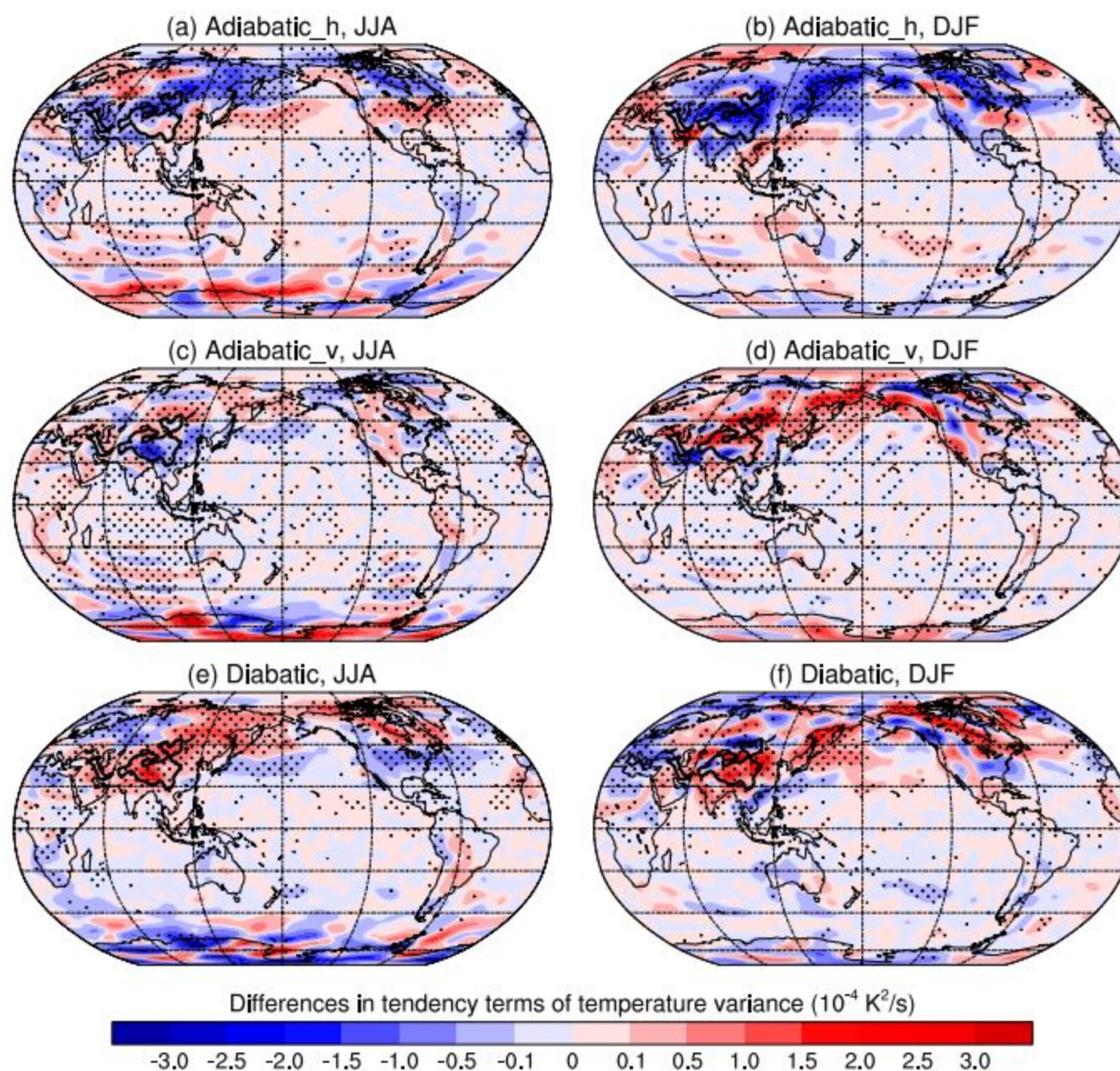
FIG. 6. As in Fig. 5, but for differences determined using CESM simulations TPnosh − noTP, which represents the mechanical effect of the TP.

variability during boreal summer (Figs. 1c and 7a,c,e), counteracting the vertical-motion-induced temperature modification upstream of the TP as well as the diabatic process over northern Eurasia. The horizontal temperature advection also dominated the decrease over the North Pacific and the tripole pattern over North America. During boreal winter, the suppressed temperature variability to the northeast of the TP was explained by the two adiabatic processes, with the horizontal temperature advection covering a wider proportion of the region. Strictly speaking, high-frequency temperature variability changes induced by the TP cannot be simply attributed to one single process. However, taken all together, over most regions across the globe, it was the horizontal temperature advection that achieved dominance, whether it was boreal winter when the mechanical effect was dominant or boreal summer when the thermal effect outweighed the mechanical effect. As for the roughly opposite effects of the TP's mechanical and thermal forcings on high-frequency temperature variability (Figs. 1 and 2), the counteraction between the horizontal

temperature advection and diabatic process played crucial roles (Figs. 6 and 7).

The roles of the climatological mean temperature gradient (thermodynamical factor) and EKE (dynamical factor) were investigated further to clarify the mechanisms underlying the effect of the horizontal temperature advection. Specifically, we compared the signs of the differences in high-frequency temperature variance with those of the norm of the climatological mean temperature gradient and EKE at 850 hPa (Figs. 8 and C1; see appendix C). Since the increased mean temperature gradient (Figs. 8d–f) was opposite to the weakened horizontal temperature advection term for temperature variance in the east and northeast of the TP (Fig. 6b), the mechanical-forcing-dominated negative changes in the dynamical factor (Fig. 4) were responsible for the decrease in the temperature variance in the east and northeast of the TP (Fig. 2). Furthermore, the reduced dynamical factor suggests that the mechanical forcing of the TP weakened energetic eddies in the westerly jets in winter (Lutsko et al. 2019).
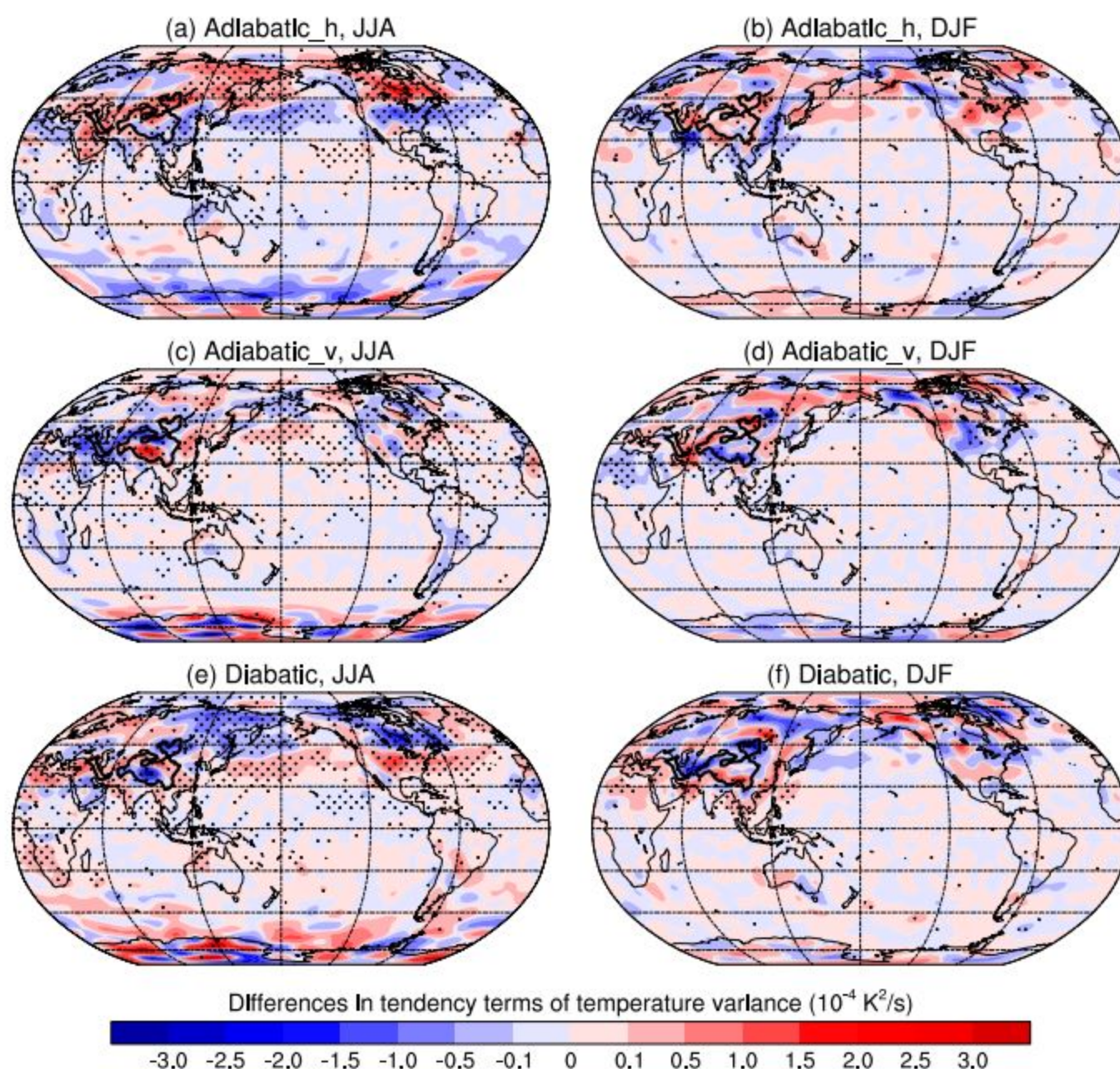
FIG. 7. As in Fig. 5, but for differences determined using CESM simulations CTRL − TPnosh, which represents the thermal effect of the TP.

## 4. Conclusions and discussion

This study aids in understanding the impact of TP topography on global high-frequency temperature and circulation variability. The key contributions of this study are as follows: The specific effects of mechanical and thermal forcings are explored separately, in addition to the overall effect of the TP. The seasonal characteristics are demonstrated. This study shows that the TP significantly influenced global high-frequency temperature and circulation variability in both boreal winter and summer. Furthermore, the contributions of physical processes, that is, horizontal temperature advection, vertical-motion-induced temperature modification, and diabatic processes, to the impact of the TP on global high-frequency temperature variability are explicitly revealed.

The following are the key conclusions: The changes in high-frequency variability induced by the TP mechanical and thermal forcing are generally counteracted by each other in patterns. Thermal forcing is dominant for high-frequency temperature variability in boreal summer, whereas mechanical forcing is

dominant in winter. Mechanical forcing dominated changes in the high-frequency variability of atmospheric circulation, as represented by the EKE, during both winter and summer. Since the effects of the TP on the high-frequency temperature and circulation variability are not constrained to its vicinity, they could extend to remote regions such as America. The TP thermal-forcing-induced change in temperature variability is dominant in boreal summer, while the TP mechanical-forcing-induced change is dominant in winter. For the majority of the regions across the globe, the main contribution of the horizontal temperature advection to the TP's mechanical and thermal effects was recognized. Moreover, the opposite mechanical and thermal effects of the TP on temperature variability are also attributed to horizontal temperature advection.

The experiments examined in this study are not fully coupled simulations, in which air–sea interactions were not active. The air–sea interactions have been suggested to be crucial for modulating the influence of the TP on global climate
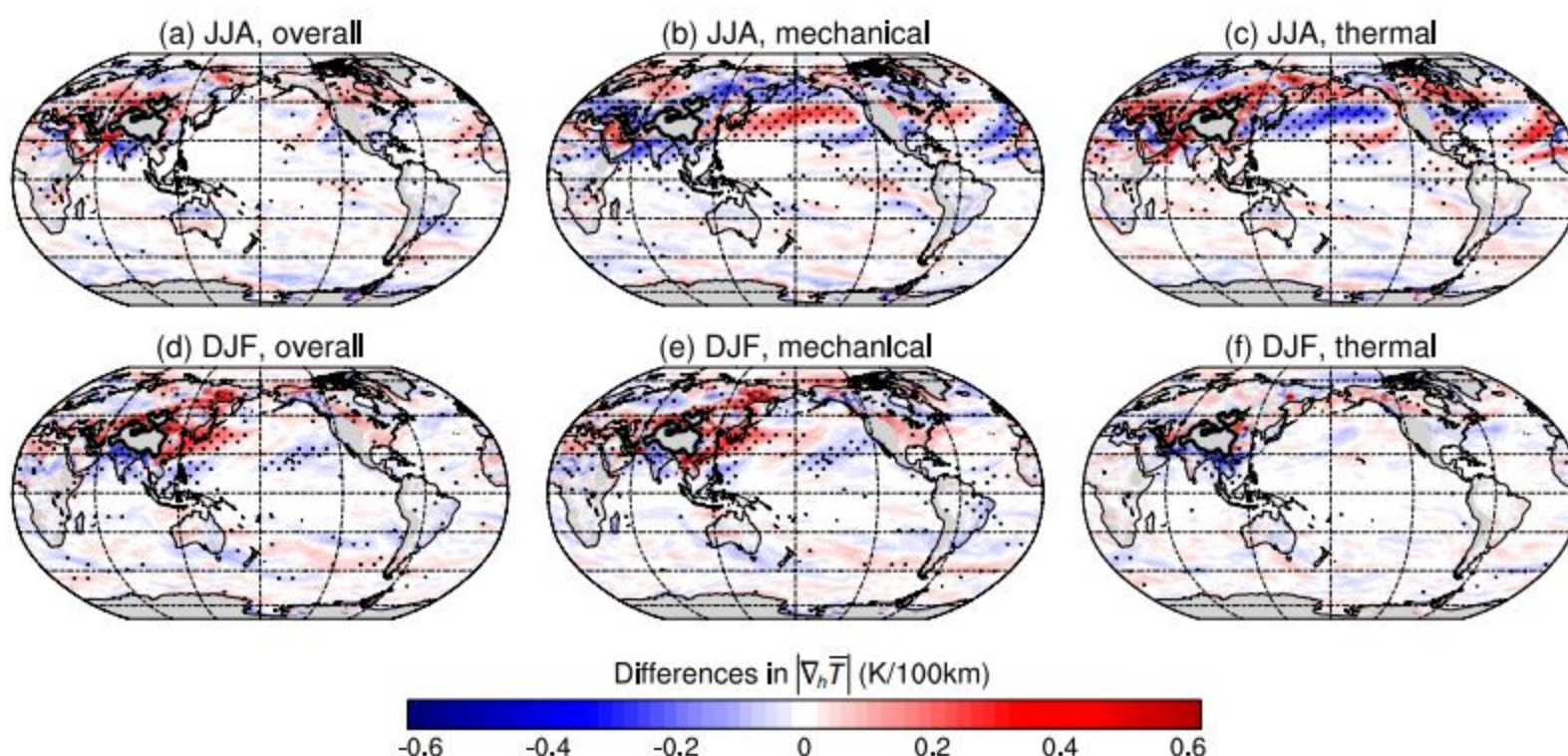
FIG. 8. Differences in the norm of the gradient of climatological mean air temperature $[|\nabla_h \overline{T}|$, Eq. (5)] at 850 hPa in JJA based on CESM, version 2.1.3, for 2000–14, determined using (a) CTRL − noTP, (b) TPnosh − noTP, and (c) CTRL − TPnosh, which represent the overall, mechanical, and thermal influences of the TP, respectively. (d)–(f) As in (a)–(c), but for DJF. The dots indicate the statistical significance at the 95% confidence level. The black contour indicates 1.5 km of elevation.

(Kitoh 2004; Baldwin et al. 2019; He et al. 2019; Lu et al. 2019; Sun et al. 2019; Xie et al. 2023b,c; Yang and Wang 2023). For example, He et al. (2019) demonstrated that the air–sea interactions over the tropical Indian Ocean counteract the effect of TP's thermal forcing. Xie et al. (2023b) found that the Pacific and Atlantic Oceans act as oceanic repeaters in the subtopics that amplify the influence of the TP across the globe. Therefore, the role of air–sea interactions should be explored and investigated further when assessing the effect of TP forcing. Carrying out simulation studies, that is, comparing atmosphere-only simulations with ones coupled with oceans, and then applying the observational constraint concept (Huang et al. 2016; Xie et al. 2023b), in which simulated variations should range within the observed, could be one of the possible routes.

Weather in midlatitudes is closely related to the high-frequency temperature and circulation variability, as synoptic-scale transient variance maxima signifies the preferred geographical passage of cyclones or storm tracks (Blackmon et al. 1977). The positions and intensities of storm tracks can be affected by land–sea differences, orographic forcing, and eddy-induced diabatic heating (Trenberth 1991). This study shows that the mechanical forcing of the TP significantly influenced the EKE, which is related to the energetic eddies, as well as storm tracks. Yang et al. (2022) also revealed that mechanical forcing of the TP weakens downstream North Pacific storm tracks not only in boreal winter but also in other seasons. This is explained by altered baroclinic energy conversion, East Asian trough, and stationary eddy heat flux. Therefore, the TP's mechanical-forcing-induced EKE changes also imply the TP's influences on storminess, as well as midlatitude weather extremes.

Nevertheless, much of the current TP topography formed by about 8 million years ago (Harrison et al. 1992). Under the current quasi-fixed topography, the thermal forcing of the TP has become the active stimulus for modern climate variations. The TP thermal forcing has been shown to vary greatly throughout time scales ranging from seasonal to decadal (Liu et al. 2012; Zhao et al. 2018). The TP thermal forcing has also been projected to increase with continuous global warming (M. Wang et al. 2019). Thus, as implied by this study, the influence of the TP thermal forcing on observed and future changes in the high-frequency temperature and circulation variability, as well as relevant weather extremes, is an important issue that needs to be addressed. In this regard, Tan et al. (2023) has shown a link between TP thermal forcing and heatwaves in China.

*Data availability statement.* ERA5 data can be accessed at https://cds.climate.copernicus.eu/cdsapp#!/dataset/reanalysis-era5-single-levels?tab=form and https://cds.climate.copernicus.eu/cdsapp#!/dataset/reanalysis-era5-single-levels?tab=form. MERRA-2 data can be accessed at https://disc.gsfc.nasa.gov/datasets?project=MERRA-2. NCEP-2 data can be obtained from https://psl.noaa.gov/data/gridded/data.ncep.reanalysis2.html. GMMIP data are available at https://esgf-node.llnl.gov/search/cmip6/. Data from the CESM simulations and codes are available at https://doi.org/10.5281/zenodo.10894681.

## APPENDIX A

### Observed Global High-Frequency Temperature and Circulation Variability Features and CESM Model Performance

The control run simulated the observed distribution of the high-frequency temperature variance $\overline{T'^2}$ in both summer and winter (Fig. A1). For example, the higher variabilities over land relative to those over the ocean and in winter for each hemisphere relative to those in summer agreed well between the control run and observations. Furthermore, regional features such as large variances in Siberia and Alaska in the Northern Hemisphere and along the Antarctic coast were also highly consistent between simulations and observations. As for the magnitude, temperature variability was overall higher in the ERA5 and MERRA-2 observations compared to the model. This seems especially true over Europe, Australia, North/South Africa, and South America in JJA and over India, North Africa, Australia, TP, Siberia, and South America in DJF. The NCEP-2 results were overall higher than those in the model and the other reanalysis datasets. For these reasons, the differences between CESM and averaged observations were negative for the regions mentioned above. Despite detailed differences in magnitude, the model performed well in simulating the observed high-frequency atmospheric variability reflected by the temperature.

Figure A2 shows the EKE patterns simulated by the control run and those in the observations. The patterns are similar, such as the occurrence of high EKE in the winter hemisphere, particularly over the mid–high latitudes of the Pacific, Atlantic, and Southern Oceans. The characteristics of the storm tracks in both hemispheres, such as seasonality and regional magnitudes reflected by EKE, in simulations were consistent with those observed in ERA5 and MERRA-2 (Blackmon et al. 1977; Trenberth 1991; Hoskins and Hodges 2019a,b). NCEP-2 resembled ERA5 and MERRA-2 in patterns and seasonality, while the magnitudes were much smaller. The CESM − Obs differences in EKE were generally small and they were relatively larger over the North Pacific in boreal summer because the simulated EKE was smaller than that in all the reanalysis data; the differences were discernible over the North Pacific in winter and not over the Southern Oceans during both summer and winter as well as over the North Atlantic in boreal winter for the reason that the variations across the reanalysis datasets were even larger than those between the control simulation and observations there.

Figure A3 exhibits great consistency between CESM and GMMIP in simulating near-surface air temperature and 500-hPa geopotential height. A large temperature decrease is seen over the TP and its surroundings after the drastic tectonic uplift of the geography (Figs. A3b,e). In contrast, the thermal forcing of the TP induced temperature increments there (Figs. A3c,f). Outside the area, although the magnitude became far less, the most prominent changes in near-surface temperature occurred in North America. The overall effect caused a reduction in temperature over Eurasia and a rise over India and Arabia. The mechanical effect of the TP decreased the 500-hPa geopotential height downstream but remarkably increased it to the north and south of the topography across the globe (Figs. A3h,k). The thermal effect of the TP formed a belt of geopotential height enhancement downstream and upstream (Figs. A3i,l). The TP overall escalated global geopotential height (the slight decrease downstream of the TP failed the significance test), especially in the mid- and high latitudes of the Northern Hemisphere.
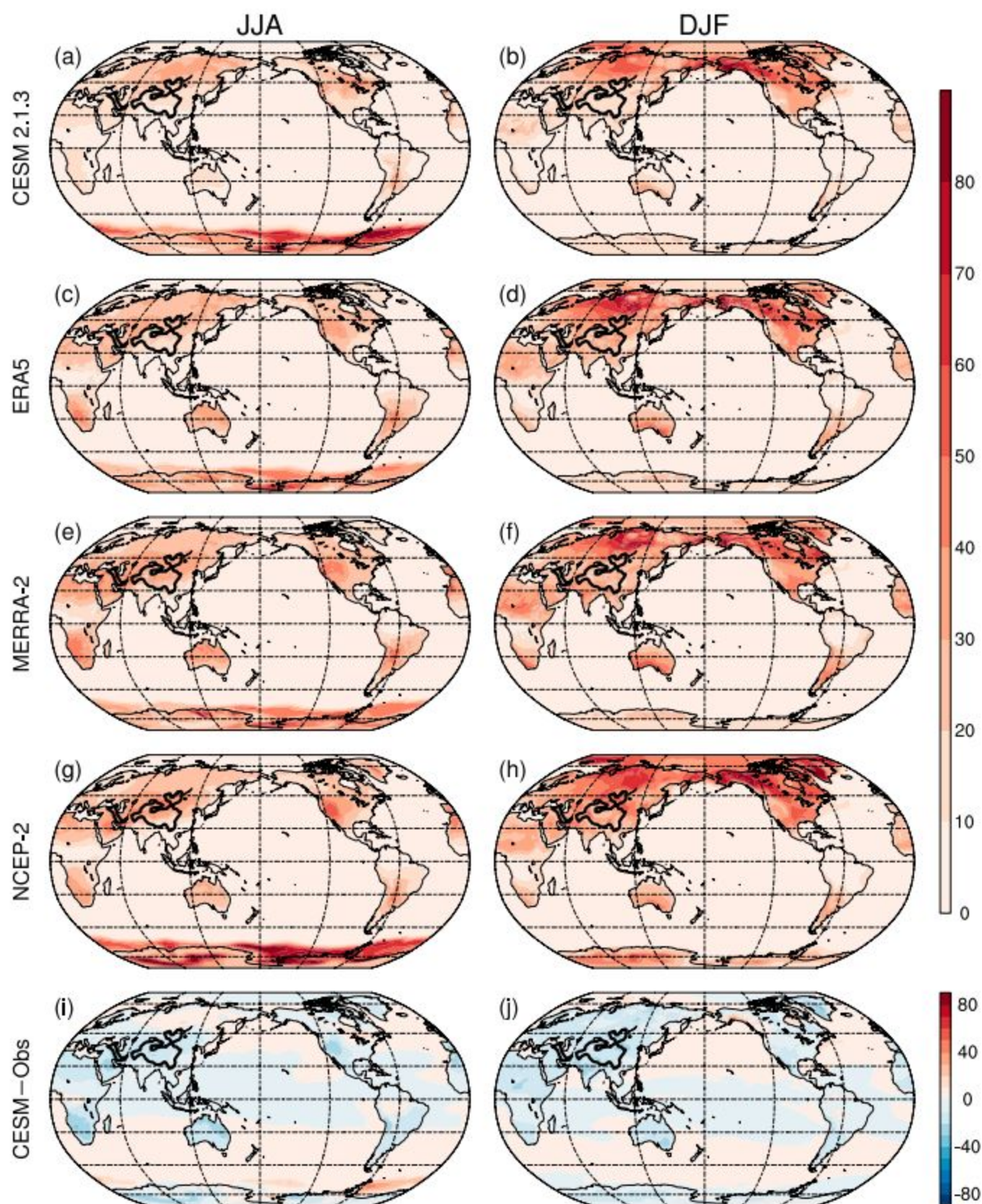
FIG. A1. Climatology of the high-frequency variance of near-surface air temperature $[\overline{T'^2}$; K$^2$; Eq. (1)] in (a) JJA and (b) DJF based on CTRL simulation of CESM, version 2.1.3, for 2000–14. (c)–(f) and (g),(h) As in (a),(b), but for ERA5, MERRA-2, and NCEP-2 reanalysis data, respectively. (i),(j) Differences using CESM minus the average of the three reanalysis data (Obs). The black contour indicates 1.5 km of elevation.
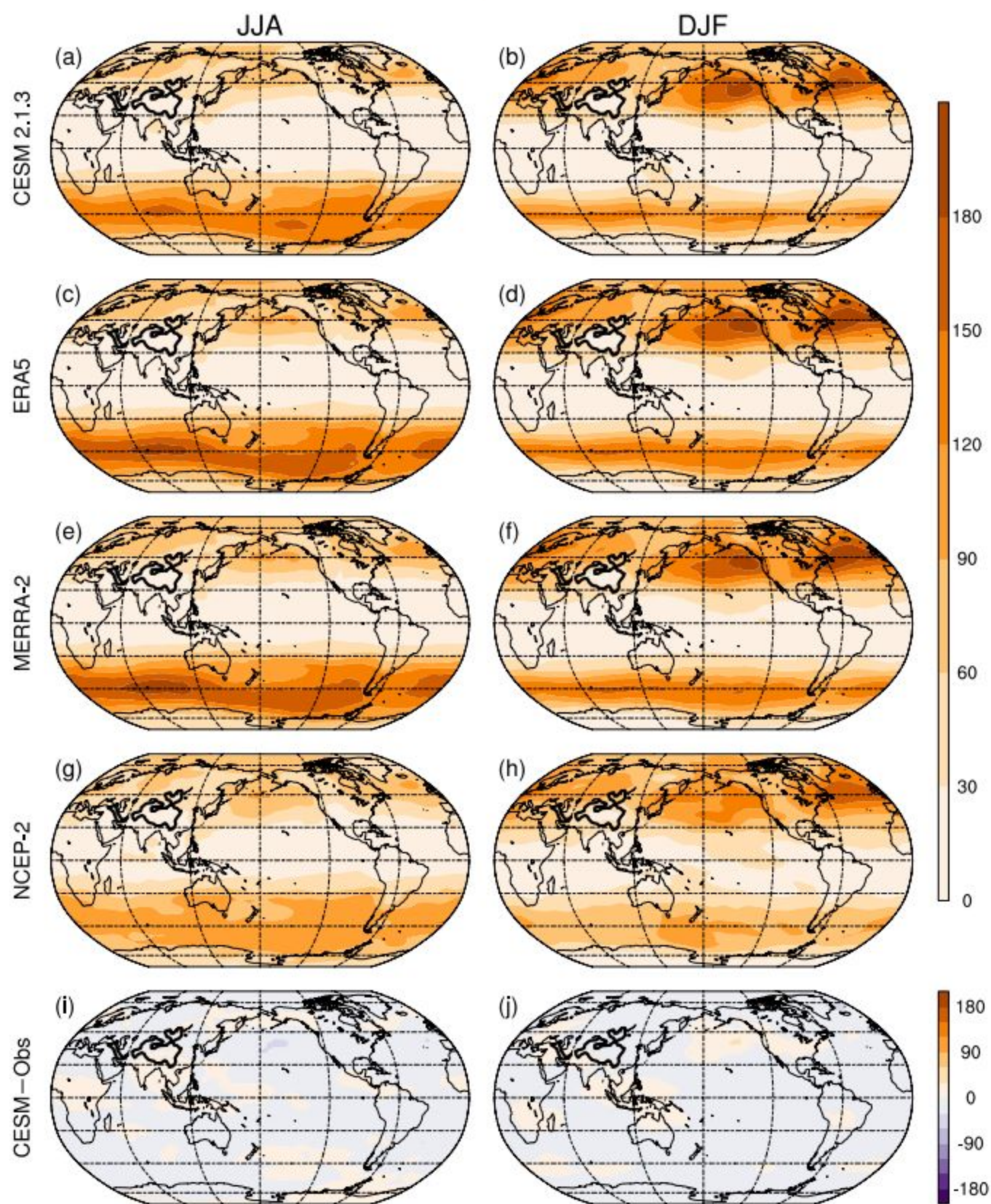
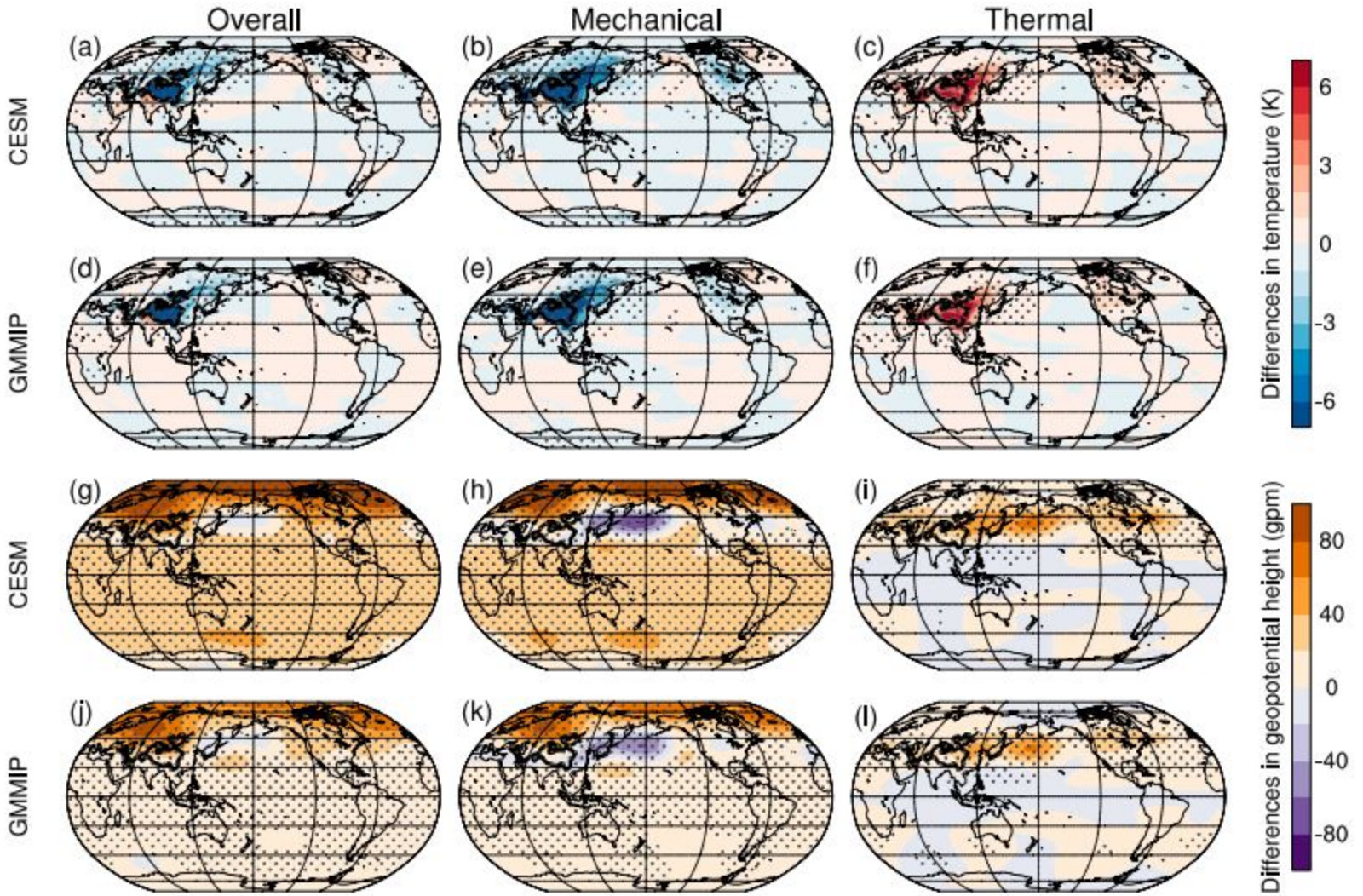Fig. A2. As in Fig. A1, but for EKE [$m^2 s^{-2}$; Eq. (2)] at 500 hPa.

FIG. A3. Differences in annual mean near-surface air temperature for 1979–2014 determined using (a) CTRL − noTP, (b) TPnosh − noTP, and (c) CTRL − TPnosh, which represent the overall, mechanical, and thermal influences of the TP, respectively, based on CESM simulations. (d)–(f) As in (a)–(c), but for results based on GMMIP simulations. The GMMIP results were the average of FGOALS-f3-L and FIO-ESM-2-0. The dots indicate that the difference between the two simulations is significant at the 95% confidence level. (g)–(l) As in (a)–(f), but for geopotential height at 500 hPa. The black contour indicates 1.5 km of elevation.

## APPENDIX B

### Model-Level Tendency Equation for High-Frequency Temperature Variability

Taking a time average to Eq. (3) over a monthly period gives

$$\frac{\partial \overline{T}}{\partial t} = -\overline{\mathbf{V} \cdot \nabla_h T} + \left( \overline{\omega \frac{\kappa T}{p}} - \overline{\omega_{\mathrm{ml}} \frac{\partial T}{\partial p}} \right) + \overline{\left( \frac{p}{p_0} \right)^{\kappa} \frac{d\theta}{dt}}. \quad (B1)$$

Subtracting Eq. (B1) from Eq. (3) yields

$$\frac{\partial T'}{\partial t} = -\mathbf{V} \cdot \nabla_h T + \left( \omega \frac{\kappa T}{p} - \omega_{\mathrm{ml}} \frac{\partial T}{\partial p} \right) + \left( \frac{p}{p_0} \right)^{\kappa} \frac{d\theta}{dt}$$
$$- \left[ -\overline{\mathbf{V} \cdot \nabla_h T} + \left( \overline{\omega \frac{\kappa T}{p}} - \overline{\omega_{\mathrm{ml}} \frac{\partial T}{\partial p}} \right) + \overline{\left( \frac{p}{p_0} \right)^{\kappa} \frac{d\theta}{dt}} \right]. \quad (B2)$$

Multiply Eq. (B2) by $2T'$, apply the time mean again, and with $\partial(\overline{T'^2})/\partial t = \overline{2T'(\partial T'/\partial t)}$, we obtain

$$\frac{\overline{\partial (T'^2)}}{\partial t} = -\overline{2T'(\mathbf{V} \cdot \nabla_h T)} + \overline{2T'\left( \omega \frac{\kappa T}{p} - \omega_{\mathrm{ml}} \frac{\partial T}{\partial p} \right)} + \overline{2T'\left( \frac{p}{p_0} \right)^{\kappa} \frac{d\theta}{dt}}$$
$$- \left[ -\overline{2T'\overline{\mathbf{V} \cdot \nabla_h T}} + \left( \overline{2T'\omega \frac{\overline{\kappa T}}{p}} - \overline{2T'\omega_{\mathrm{ml}} \frac{\overline{\partial T}}{\partial p}} \right) \right.$$
$$+ \left. \overline{2T'\overline{\left( \frac{p}{p_0} \right)^{\kappa} \frac{d\theta}{dt}}} \right]. \quad (B3)$$

The last four terms of Eq. (B3) equal zero, so the equation becomes Eq. (4).

The climatological counterbalance of the adiabatic horizontal temperature advection, adiabatic vertical-motion-induced temperature modification, and diabatic terms resulted in an almost-zero change in the local tendency of the temperature variability (Fig. B1). The horizontal temperature advection coincided with CESM-simulated high-frequency temperature variability in pattern during both boreal summer and winter (Figs. A1a,b and B1c,d) and its sign was positive among all the regions of high values, suggesting a possible dominant contribution of horizontal temperature advection to the climatological temperature variability. The diabatic process counteracted the horizontal temperature advection and is of importance. The vertical-motion-induced
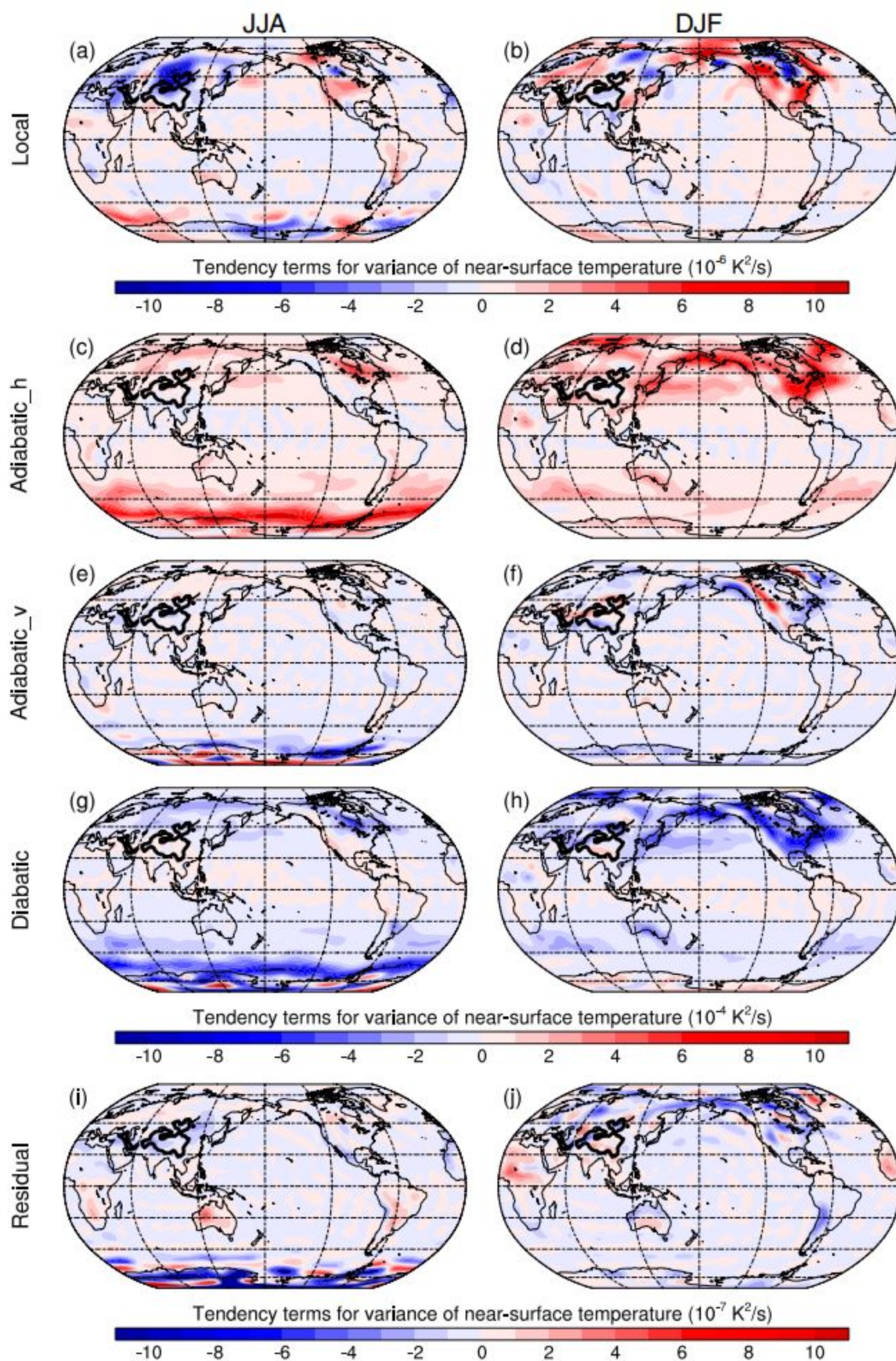
FIG. B1. Climatology of tendency for the high-frequency variance of near-surface air temperature [Eq. (4)] in JJA based on the CESM CTRL run for 2000–14. (a) Local, (c) adiabatic_h, (e) adiabatic_v, (g) diabatic, and (i) residual terms. The residual term is calculated as the left-hand term minus the right-hand terms of Eq. (4). (b),(d),(f),(h),(j) As in (a),(c),(e),(g),(i), but for DJF. The black contour indicates 1.5 km of elevation.

temperature modification mainly worked around rough terrain in winter.

## APPENDIX C

### High-Frequency Temperature Variance and EKE at 850 hPa

The spatial patterns of changes in high-frequency temperature variance $\overline{T'^2}$ and EKE at 850 hPa (Fig. C1) were very similar to the respective change patterns of near-surface $\overline{T'^2}$

and 500-hPa EKE under the overall effect of the TP. Only a few regional differences existed around the Middle East (Figs. 1a and C1a), Africa (Figs. 2a and C1b), northern Europe, and northwestern Russia (Figs. 4a and C1d). Except for these regions during corresponding seasons, the horizontal-advection-induced changes in near-surface temperature variance can be evaluated in comparison with changes in 850-hPa mean temperature gradient (thermal–dynamical factor) and 500-hPa EKE (dynamical factor).
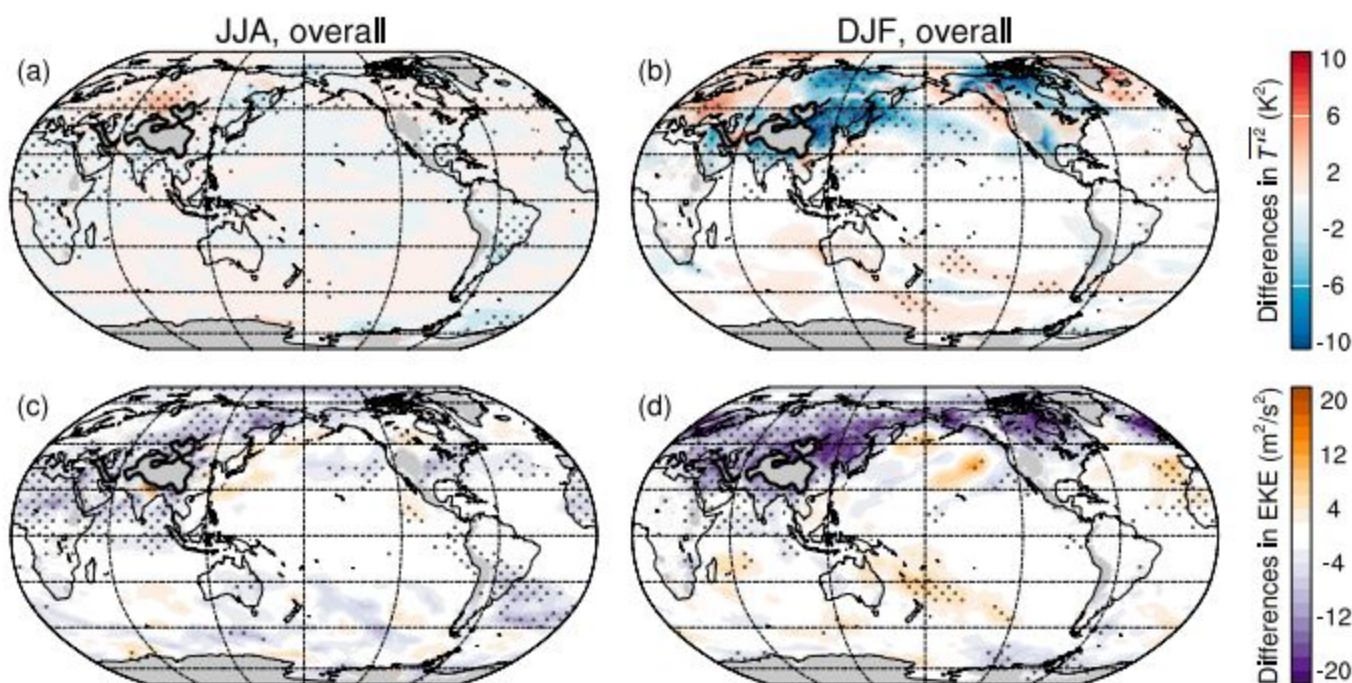


FIG. C1. Differences in $\overline{T'^2}$ at 850 hPa determined using CESM simulations CTRL − noTP in (a) JJA and (b) DJF for 2000–14, which represent the overall influences of the TP. (c),(d) As in (a),(b), but for EKE at 850 hPa. The dots indicate the statistical significance at the 95% confidence level. The black contour indicates 1.5 km of elevation.

## REFERENCES

Baldwin, J. W., G. A. Vecchi, and S. Bordoni, 2019: The direct and ocean-mediated influence of Asian orography on tropical precipitation and cyclones. *Climate Dyn.*, **53**, 805–824, https://doi.org/10.1007/s00382-019-04615-5.

Bao, Y., Z. Song, and F. Qiao, 2020: FIO-ESM version 2.0: Model description and evaluation. *J. Geophys. Res. Oceans*, **125**, e2019JC016036, https://doi.org/10.1029/2019JC016036.

Blackmon, M. L., J. M. Wallace, N.-C. Lau, and S. L. Mullen, 1977: An observational study of the Northern Hemisphere wintertime circulation. *J. Atmos. Sci.*, **34**, 1040–1053, https://doi.org/10.1175/1520-0469(1977)034<1040:AOSOTN>2.0.CO;2.

Bolin, B., 1950: On the influence of the Earth's orography on the general character of the westerlies. *Tellus*, **2A**, 184–195, https://doi.org/10.3402/tellusa.v2i3.8547.

Boos, W. R., and Z. Kuang, 2010: Dominant control of the South Asian monsoon by orographic insulation versus plateau heating. *Nature*, **463**, 218–222, https://doi.org/10.1038/nature08707.

Chiang, J. C. H., W. Kong, C. H. Wu, and D. S. Battisti, 2020: Origins of East Asian summer monsoon seasonality. *J. Climate*, **33**, 7945–7965, https://doi.org/10.1175/JCLI-D-19-0888.1.

Dai, A., and J. Deng, 2021: Arctic amplification weakens the variability of daily temperatures over northern middle-high latitudes. *J. Climate*, **34**, 2591–2609, https://doi.org/10.1175/JCLI-D-20-0514.1.

Danabasoglu, G., and Coauthors, 2020: The Community Earth System Model version 2 (CESM2). *J. Adv. Model. Earth Syst.*, **12**, e2019MS001916, https://doi.org/10.1029/2019MS001916.

Eyring, V., S. Bony, G. A. Meehl, C. A. Senior, B. Stevens, R. J. Stouffer, and K. E. Taylor, 2016: Overview of the Coupled Model Intercomparison Project Phase 6 (CMIP6) experimental design and organization. *Geosci. Model Dev.*, **9**, 1937–1958, https://doi.org/10.5194/gmd-9-1937-2016.

Fallah, B., U. Cubasch, K. Prömmel, and S. Sodoudi, 2016: A numerical model study on the behaviour of Asian summer monsoon and AMOC due to orographic forcing of Tibetan Plateau. *Climate Dyn.*, **47**, 1485–1495, https://doi.org/10.1007/s00382-015-2914-5.

Gelaro, R., and Coauthors, 2017: The Modern-Era Retrospective Analysis for Research and Applications, version 2 (MERRA-2). *J. Climate*, **30**, 5419–5454, https://doi.org/10.1175/JCLI-D-16-0758.1.

Harrison, T., P. Copeland, W. S. F. Kidd, and A. Yin, 1992: Raising Tibet. *Science*, **255**, 1663–1670, https://doi.org/10.1126/science.255.5052.1663.

He, B., Y. Liu, G. Wu, Z. Wang, and Q. Bao, 2019: The role of air–sea interactions in regulating the thermal effect of the Tibetan–Iranian Plateau on the Asian summer monsoon. *Climate Dyn.*, **52**, 4227–4245, https://doi.org/10.1007/s00382-018-4377-y.

——, and Coauthors, 2020: CAS FGOALS-f3-L model datasets for CMIP6 GMMIP tier-1 and tier-3 experiments. *Adv. Atmos. Sci.*, **37**, 18–28, https://doi.org/10.1007/s00376-019-9085-y.

Held, I. M., and M. Ting, 1990: Orographic versus thermal forcing of stationary waves: The importance of the mean low-level wind. *J. Atmos. Sci.*, **47**, 495–500, https://doi.org/10.1175/1520-0469(1990)047<0495:OVTFOS>2.0.CO;2.

Hersbach, H., and Coauthors, 2020: The ERA5 global reanalysis. *Quart. J. Roy. Meteor. Soc.*, **146**, 1999–2049, https://doi.org/10.1002/qj.3803.

Hoskins, B. J., and K. I. Hodges, 2019a: The annual cycle of Northern Hemisphere storm tracks. Part I: Seasons. *J. Climate*, **32**, 1743–1760, https://doi.org/10.1175/JCLI-D-17-0870.1.

——, and ——, 2019b: The annual cycle of Northern Hemisphere storm tracks. Part II: Regional detail. *J. Climate*, **32**, 1761–1775, https://doi.org/10.1175/JCLI-D-17-0871.1.

Huang, J., H. Yu, X. Guan, G. Wang, and R. Guo, 2016: Accelerated dryland expansion under climate change. *Nat. Climate Change*, **6**, 166–171, https://doi.org/10.1038/nclimate2837.

——, and Coauthors, 2023: Global climate impacts of land-surface and atmospheric processes over the Tibetan Plateau. *Rev. Geophys.*, **61**, e2022RG000771, https://doi.org/10.1029/2022RG000771.

Kanamitsu, M., W. Ebisuzaki, J. Woollen, S.-K. Yang, J. J. Hnilo, M. Fiorino, and G. L. Potter, 2002: NCEP–DOE AMIP-II Reanalysis (R-2). *Bull. Amer. Meteor. Soc.*, **83**, 1631–1644, https://doi.org/10.1175/BAMS-83-11-1631.

Kitoh, A., 2004: Effects of mountain uplift on East Asian summer climate investigated by a coupled atmosphere–ocean GCM. *J. Climate*, **17**, 783–802, https://doi.org/10.1175/1520-0442(2004)017<0783:EOMUOE>2.0.CO;2.

Laguë, M. M., G. B. Bonan, and A. L. S. Swann, 2019: Separating the impact of individual land surface properties on the terrestrial surface energy budget in both the coupled and uncoupled land–atmosphere system. *J. Climate*, **32**, 5725–5744, https://doi.org/10.1175/JCLI-D-18-0812.1.

Li, L., and R. Zhang, 2023: Evolution mechanisms, impacts, and variations of the vortices originated from the Tibetan Plateau. *Earth-Sci. Rev.*, **242**, 104463, https://doi.org/10.1016/j.earscirev.2023.104463.

——, ——, P. Wu, M. Wen, and J. Duan, 2020: Roles of Tibetan Plateau vortices in the heavy rainfall over southwestern China in early July 2018. *Atmos. Res.*, **245**, 105059, https://doi.org/10.1016/j.atmosres.2020.105059.

Lin, H., and Z. Wu, 2011: Contribution of the autumn Tibetan Plateau snow cover to seasonal prediction of North American winter temperature. *J. Climate*, **24**, 2801–2813, https://doi.org/10.1175/2010JCLI3889.1.

Liu, Y., B. Hoskins, and M. Blackburn, 2007: Impact of Tibetan orography and heating on the summer flow over Asia. *J. Meteor. Soc. Japan*, **85B**, 1–19, https://doi.org/10.2151/jmsj.85B.1.

——, G. Wu, J. Hong, B. Dong, A. Duan, Q. Bao, and L. Zhou, 2012: Revisiting Asian monsoon formation and change associated with Tibetan Plateau forcing: II. Change. *Climate Dyn.*, **39**, 1183–1195, https://doi.org/10.1007/s00382-012-1335-y.

——, Z. Wang, H. Zhuo, and G. Wu, 2017: Two types of summertime heating over Asian large-scale orography and excitation of potential-vorticity forcing II. Sensible heating over Tibetan-Iranian Plateau. *Sci. China Earth Sci.*, **60**, 733–744, https://doi.org/10.1007/s11430-016-9016-3.

——, M. Lu, H. Yang, A. Duan, B. He, S. Yang, and G. Wu, 2020: Land–atmosphere–ocean coupling associated with the Tibetan Plateau and its climate impacts. *Natl. Sci. Rev.*, **7**, 534–552, https://doi.org/10.1093/nsr/nwaa011.

Lu, M., B. Huang, Z. Li, S. Yang, and Z. Wang, 2019: Role of Atlantic air–sea interaction in modulating the effect of Tibetan Plateau heating on the upstream climate over Afro-Eurasia–Atlantic regions. *Climate Dyn.*, **53**, 509–519, https://doi.org/10.1007/s00382-018-4595-3.

Lutsko, N. J., and I. M. Held, 2016: The response of an idealized atmosphere to orographic forcing: Zonal versus meridional propagation. *J. Atmos. Sci.*, **73**, 3701–3718, https://doi.org/10.1175/JAS-D-16-0021.1.

——, J. W. Baldwin, and T. W. Cronin, 2019: The impact of large-scale orography on Northern Hemisphere winter synoptic temperature variability. *J. Climate*, **32**, 5799–5814, https://doi.org/10.1175/JCLI-D-19-0129.1.

Ma, T., G. Wu, Y. Liu, and J. Mao, 2022: Abnormal warm sea-surface temperature in the Indian Ocean, active potential vorticity over the Tibetan Plateau, and severe flooding along the Yangtze River in summer 2020. *Quart. J. Roy. Meteor. Soc.*, **148**, 1001–1019, https://doi.org/10.1002/qj.4243.

Manabe, S., and A. J. Broccoli, 1990: Mountains and arid climates of middle latitudes. *Science*, **247**, 192–195, https://doi.org/10.1126/science.247.4939.192.

Molnar, P., W. R. Boos, and D. S. Battisti, 2010: Orographic controls on climate and paleoclimate of Asia: Thermal and mechanical roles for the Tibetan Plateau. *Annu. Rev. Earth Planet. Sci.*, **38**, 77–102, https://doi.org/10.1146/annurev-earth-040809-152456.

NCAR, 2015: The NCAR Command Language Version 6.3.0. UCAR/NCAR/CISL/TDD, https://doi.org/10.5065/D6WD3XH5.

Ping, Z., and C. Longxun, 2001: Interannual variability of atmospheric heat source/sink over the Qinghai–Xizang (Tibetan) Plateau and its relation to circulation. *Adv. Atmos. Sci.*, **18**, 106–116, https://doi.org/10.1007/s00376-001-0007-3.

Queney, P., 1948: The problem of air flow over mountains: A summary of theoretical studies. *Bull. Amer. Meteor. Soc.*, **29**, 16–26, https://doi.org/10.1175/1520-0477-29.1.16.

Rahmstorf, S., and D. Coumou, 2011: Increase of extreme events in a warming world. *Proc. Natl. Acad. Sci. USA*, **108**, 17 905–17 909, https://doi.org/10.1073/pnas.1101766108.

Schär, C., P. L. Vidale, D. Lüthi, C. Frei, C. Häberli, M. A. Liniger, and C. Appenzeller, 2004: The role of increasing temperature variability in European summer heatwaves. *Nature*, **427**, 332–336, https://doi.org/10.1038/nature02300.

Schneider, T., T. Bischoff, and H. Płotka, 2015: Physics of changes in synoptic midlatitude temperature variability. *J. Climate*, **28**, 2312–2331, https://doi.org/10.1175/JCLI-D-14-00632.1.

Sheng, C., and Coauthors, 2021: Characteristics of the potential vorticity and its budget in the surface layer over the Tibetan Plateau. *Int. J. Climatol.*, **41**, 439–455, https://doi.org/10.1002/joc.6629.

Son, J.-H., K.-H. Seo, and B. Wang, 2019: Dynamical control of the Tibetan Plateau on the East Asian summer monsoon. *Geophys. Res. Lett.*, **46**, 7672–7679, https://doi.org/10.1029/2019GL083104.

Su, B., D. Jiang, R. Zhang, P. Sepulchre, and G. Ramstein, 2018: Difference between the North Atlantic and Pacific meridional overturning circulation in response to the uplift of the Tibetan Plateau. *Climate Past*, **14**, 751–762, https://doi.org/10.5194/cp-14-751-2018.

Sun, R., A. Duan, L. Chen, Y. Li, Z. Xie, and Y. Zhao, 2019: Interannual variability of the North Pacific mixed layer associated with the spring Tibetan Plateau thermal forcing. *J. Climate*, **32**, 3109–3130, https://doi.org/10.1175/JCLI-D-18-0577.1.

Tan, Z., Y. Liu, T. Shao, R. Luo, M. Luo, and Y. Xie, 2023: Association between Tibetan heat sources and heat waves in China. *J. Climate*, **36**, 7905–7924, https://doi.org/10.1175/JCLI-D-22-0568.1.

Trenberth, K. E., 1991: Storm tracks in the Southern Hemisphere. *J. Atmos. Sci.*, **48**, 2159–2178, https://doi.org/10.1175/1520-0469(1991)048<2159:STITSH>2.0.CO;2.

Wang, L., H. Yang, Q. Wen, Y. Liu, and G. Wu, 2023: The Tibetan Plateau's far-reaching impacts on Arctic and Antarctic climate: Seasonality and pathways. *J. Climate*, **36**, 1399–1414, https://doi.org/10.1175/JCLI-D-22-0175.1.

Wang, M., and Coauthors, 2019: Recent recovery of the boreal spring sensible heating over the Tibetan Plateau will continue in CMIP6 future projections. *Environ. Res. Lett.*, **14**, 124066, https://doi.org/10.1088/1748-9326/ab57a3.

Wang, Z., A. Duan, and S. Yang, 2019: Potential regulation on the climatic effect of Tibetan Plateau heating by tropical air–sea coupling in regional models. *Climate Dyn.*, **52**, 1685–1694, https://doi.org/10.1007/s00382-018-4218-z.

Wu, G., and Coauthors, 2007: The influence of mechanical and thermal forcing by the Tibetan Plateau on Asian climate. *J. Hydrometeor.*, **8**, 770–789, https://doi.org/10.1175/JHM609.1.

——, T. Ma, Y. Liu, and Z. Jiang, 2020: PV-Q perspective of cyclogenesis and vertical velocity development downstream of the Tibetan Plateau. *J. Geophys. Res. Atmos.*, **125**, e2019JD030912, https://doi.org/10.1029/2019JD030912.

Wu, G.-X., 1984: The nonlinear response of the atmosphere to large-scale mechanical and thermal forcing. *J. Atmos. Sci.*, **41**, 2456–2476, https://doi.org/10.1175/1520-0469(1984)041<2456:TNROTA>2.0.CO;2.

Wu, Z., P. Zhang, H. Chen, and Y. Li, 2016: Can the Tibetan Plateau snow cover influence the interannual variations of Eurasian heat wave frequency? *Climate Dyn.*, **46**, 3405–3417, https://doi.org/10.1007/s00382-015-2775-y.s.

Xiang, S., Y. Li, D. Li, and S. Yang, 2013: An analysis of heavy precipitation caused by a retracing plateau vortex based on TRMM data. *Meteor. Atmos. Phys.*, **122**, 33–45, https://doi.org/10.1007/s00703-013-0269-1.

Xie, Y., H. Nie, and Y. He, 2022: Extratropical climate change during periods before and after an Arctic ice-free summer. *Earth's Future*, **10**, e2022EF002881, https://doi.org/10.1029/2022EF002881.

——, G. Wu, Y. Liu, J. Huang, C. Sheng, and Y. Wu, 2023a: A potential vorticity budget view of the atmospheric circulation climatology over the Tibetan Plateau. *Int. J. Climatol.*, **43**, 2031–2049, https://doi.org/10.1002/joc.7960.

——, and Coauthors, 2023b: Oceanic repeaters boost the global climatic impact of the Tibetan Plateau. *Sci. Bull.*, **68**, 2225–2235, https://doi.org/10.1016/j.scib.2023.07.019.

——, J. Huang, G. Wu, N. Lei, and Y. Liu, 2023c: Enhanced Asian warming increases Arctic amplification. *Environ. Res. Lett.*, **18**, 034041, https://doi.org/10.1088/1748-9326/acbdb1.

Yanai, M., C. Li, and Z. Song, 1992: Seasonal heating of the Tibetan Plateau and its effects on the evolution of the Asian summer monsoon. *J. Meteor. Soc. Japan*, **70**, 319–351, https://doi.org/10.2151/jmsj1965.70.1B_319.

Yang, H., and Q. Wen, 2020: Investigating the role of the Tibetan Plateau in the formation of Atlantic meridional overturning circulation. *J. Climate*, **33**, 3585–3601, https://doi.org/10.1175/JCLI-D-19-0205.1.

——, X. Shen, J. Yao, and Q. Wen, 2020: Portraying the Impact of the Tibetan Plateau on global climate. *J. Climate*, **33**, 3565–3583, https://doi.org/10.1175/JCLI-D-18-0734.1.

——, R. Jiang, Q. Wen, Y. Liu, G. Wu, and J. Huang, 2024: The role of mountains in shaping the global meridional overturning circulation. *Nat. Commun.*, **15**, 2602, https://doi.org/10.1038/s41467-024-46856-x.

Yang, M., C. Li, D. Luo, Y. Yao, X. Li, X. Chen, and Y. Lu, 2022: Mechanical and thermal impacts of the Tibetan–Iranian Plateau on the North Pacific storm track: Numerical experiments by FGOALS-f3-L. *J. Geophys. Res. Atmos.*, **127**, e2021JD035659, https://doi.org/10.1029/2021JD035659.

Yang, S., and Z. Wang, 2023: Air-sea interactions amplify the global climate effects of the Tibetan Plateau. *Sci. Bull.*, **68**, 2689–2690, https://doi.org/10.1016/j.scib.2023.09.047.

Yeh, T., 1950: The circulation of the high troposphere over China in the winter of 1945–46. *Tellus*, **2** (3), 173–183, https://doi.org/10.3402/tellusa.v2i3.8548.

Zhao, P., X. Zhou, J. Chen, G. Liu, and S. Nan, 2019: Global climate effects of summer Tibetan Plateau. *Sci. Bull.*, **64** (1), 1–3, https://doi.org/10.1016/j.scib.2018.11.019.

Zhao, Y., A. Duan, and G. Wu, 2018: Interannual variability of late-spring circulation and diabatic heating over the Tibetan Plateau associated with Indian Ocean forcing. *Adv. Atmos. Sci.*, **35**, 927–941, https://doi.org/10.1007/s00376-018-7217-4.

Zhou, T., and Coauthors, 2016: GMMIP (v1.0) contribution to CMIP6: Global monsoons model inter-comparison project. *Geosci. Model Dev.*, **9**, 3589–3604, https://doi.org/10.5194/gmd-9-3589-2016.